Diss. ETH No. 16962

Low Coherence Interferometry In Turbomachinery and Flow Velocimetry

A dissertation submitted to the
Swiss Federal Institute of Technology Zurich

for the degree of
Doctor of Science

presented by
Andreas Kempe
Dipl.-Ing. TU Dresden
born September, 7, 1977
citizen of Germany

accepted on the recommendation of
Prof. Dr.-Ing. Thomas Rösgen, supervisor
Ken Yves Haffner, co-examiner

2007

Low Coherence Interferometry In Turbomachinery and Flow Velocimetry

Published and distributed by:

Institute of Fluiddynamics
Swiss Federal Institute of Technology (ETH) Zürich
ETH Zentrum, ML H35
CH-8092 Zurich
Switzerland

http://www.ifd.mavt.ethz.ch

Printed in Switzerland by:

Repro ETH Hönggerberg
Wolfgang-Pauli-Str. 15, HIL C 45
CH-8093 Zürich
Switzerland

Acknowledgments

The work on this thesis was always inspiring and exciting, sometimes it was challenging and also attritional, but overall it was a very interesting and unforgettable experience. Its success has been made possible by the help of many other people. Thus, I want to express my gratitude to everybody for supporting me in my research.

In particular I would like to thank my supervisor Prof. Dr.-Ing. Thomas Rösgen, who has given me the chance to participate in interesting research projects and attend various international conferences. He also gave me the opportunity for a research visit at the California Institute of Technology, which was a very unique experience for me. During the daily work he has supported me with his encouragement and he has always shown his interest in my research - leading to many discussions.

I want also thank my co-supervisor Ken Y. Haffner for his fruitful recommendations to write this thesis as a summary of my research work. Particularly, I would like to express my sincere thanks to him again as my research partner within ALSTOM Power. Without his help the success of the project would not has been possible. With his unresting engagement he paved the way for tests at a full sized gas turbine. The test series at such a "hell of a machine" was a really exciting experience for me. Concerning the work together with ALSTOM Power, I have to thank for the financial support to the project, too.

A special thanks also goes to Dr. Stefan Schlamp who greatly enriched my knowledge with his exceptional insights into the academical research. The close cooperation with him in writing papers helped me overcomethis - disliked by me - aspect of the academic work. I also have to thank him for always listening to all of my new ideas, it was the fastest way to smash them down or to decide to give it a try.

Last but not least, sincere thanks go to my lovely ones: my parents and of course my girlfriend. For my parents I don´t have to enumerate what they have done for me. I just want to say: Danke! Et pour ma petite amie: je la remercie pas uniquement grâce à son ordinateur que j´ai pu utiliser pour écrire ma thése mais pour beaucoup plus! Un gros bisou!

Contents

List of Figures / Tables

Figures

Tables

Notations

All bold letters represent vectors, underlines denote the complex from. The latin letters x, y, z represent the cartesian coordinates, u, v, w the corresponding velocities in $[m/s]$.

Latin Letters

Symbol	Unit	Description
A	m^2	area
$\mathscr{A}$	–	autocorrelation function
B	T	magnetic induction
b	m	width
c, c_o	m/s	speed of light, $\sim$ in vacuum
D	C/m^2	electric displacement
d	m	distance
E	V/m	electric field strength
$\mathscr{E}$	J/Hz	energy spectral density
e	–	unit vector
$\mathscr{F}$	–	Fourier transformation function
$f_{\mathscr{P}}$	–	factor for the shape of the power spectral density
f, f_c, f_{shift}	Hz	frequency, cut-off $\sim$, $\sim$ shift
G	–	photodetector gain factor
H	A/m	magnetic field strength
h	eVs	Planck constant
I	W/m^2	electromagnetic intensity
$i_d, i_{jn}, i_p,$ i_{SAT}, i_{sn}	A	photodiode dark current, $\sim$ Johnson-Nyquist noise current, $\sim$ electric current, $\sim$ reverse saturation current, $\sim$ shot noise current
k	–	wavenumber
k_B	eV/K	Boltzmann constant
l, l_c	m	length, coherence $\sim$
m	kg	mass
m_v	–	modulation depth / visibility
NA	–	numerical aperture
NEP	$W/\sqrt{Hz}$	noise equivalent power
n, n_{eff}	–	refractive index, effective refractive index
P	–	Poynting vector
P_P	W	photodiode power
$\mathscr{P}, \hat{\mathscr{P}}$	$W/Hz, -$	power spectral density, normalized $\sim$
Q	–	bragg cell quality factor
q	C	elemental charge
Re	–	Reynolds number

continued on next page

Symbol	Unit	Description
R_λ	A/W	spectral responsivity
R_{SH}	Ω	photodiode shunt resistance
r, r_{core}	m	radius, $\sim$ of fiber core
S	A/m^2	current density
s	$-$	signal
T	K	absolute temperature
Ta	$-$	Taylor number
t, t_f	s	time, $\sim$ of flight
V	$-$	optical fiber V-parameter
V_A	V	applied bias voltage
v, v_r, v_p	m/s	velocity, relative $\sim$, particle $\sim$
V_A	V	applied bias voltage
w	J/m^3	energy density

Greek Letters

Symbol	Unit	Description
β	rad	angle
γ	$-$	self coherence function
Δ	$-$	difference
$\varepsilon, \varepsilon_o$	F/m	electric permittivity, $\sim$ in vacuum
η	$Pa\,s$	dynamic viscosity
η_q	$-$	quantum efficiency
Θ	rad	angle
κ	S/m	electric conductivity
λ, λ_o	m	light wavelength, $\sim$ in vacuum
Λ	m	acoustic wavelength
μ, μ_o	N/A^2	magnetic permeability, $\sim$ in vacuum
ρ_c	C/m^3	charge density
τ, τ_c	s	time incremental, coherence time
ξ_{broad}	$-$	broadening factor
φ	rad	phase angle
ω	Hz	2πf - angular frequency

Abbreviations

Symbol	Description
AOM	acousto-optic modulator
DSO	digital storage oscilloscope
LCI	low coherence interferometry
EFE, SFE	endoscopic front end, sensor front end
SR	self-referencing

Zusammenfassung

Diese Doktorarbeit enstand in den Jahren 2002 bis 2006 am Institut für Fluiddynamik, ETH Zürich. Die Arbeit wurde hauptsächlich durch ALSTOM Power Switzerland im Rahmen der Kooperation Center of Energy Conversion - CEC finanziert.

Es werden zwei neue Messmethoden für die Anwendung von Niedrig-Kohärenz Interferometrie vorgestellt. Zum einen konnte zum ersten Mal die *Tip Clearance* (Schaufelabstand) der ersten Laufreihe nach der Brennkammer einer Kraftwerksgasturbine unter realen Bedingungen akkurat gemessen werden. Zum anderen wurde ein neues Laser-Anemometer entwickelt, welches auf einfache Weise erlaubt Grenzschichten auf bewegten Oberflächen zu messen.

Die Entwicklung der *Tip Clearance* Messsonde war das ursprüngliche Projekt. Es wurde ein System entwickelt mit dem zeitlich aufglöste Abstandsmessungen an der ersten der Brennkammer folgenden Laufreihe einer Gasturbine durchgeführt werden können. Das Prinzip basiert auf der Interferenz zwischen dem Streulicht einer vorbeilaufenden Turbinenschaufel und dem einer Referenz im Turbinengehäuse. Zur Zeit gebräuchliche Sensoren haben entweder eine zu geringe zeitliche Auflösung, einen zu geringen Messbereich oder sind bei sehr hohen Temperaturen ($> 1000°C$) nicht dauerhaft anwendbar. Niedrig-Kohärenz Interferometrie erlaubt eine hohe zeitlich Auflösung ($\approx 1\ \mu s$) mit einer absoluten Messgenauigkeit im Bereich von unter einem hundertstel Millimeter. Der Sensorkopf kann daher in einer gekühlten Kavität platziert werden ohne an Messgenauigkeit einzubüssen. Ein faseroptischer Prototyp wurde erfolgreich auf einer Laborturbine mit Kaltgas, als auch in einer grossen Kraftwerksgasturbine (GT26-ALSTOM) getestet. Der zweite Teil dieser Doktorarbeit beschreibt die Funktionsweise dieses Sensors und gibt eine Zusammenfassung zu den Testmessungen.

Ein neues selbst referenzierende Laser-Anemometer kombiniert Techniken der Geschwindigkeitsbestimmung mit den Eigenschaften der Niedrig-Kohärenz Interferometrie (hochaufgelöste Abstandsmessung). Als neuer Ansatz sind sowohl das Messobjekt als auch die Referenz ausserhalb des Interferometers platziert und somit einander selbst referenzierend. Dies erlaubt kontaktlose Messungen von wandnahen Strömungen auch wenn sich die Oberfläche unregelmässig bewegt. Durch die Interferometereinstellung wird ohne den Sensorkopf zu bewegen die Messposition automatisch bezüglich der Oberfläche fixiert. Die absolute Genauigkeit der räumlich Auflösung liegt im Mikrometerbereich und wird durch die Eigenschaften der niedrigkohärenten Lichtquelle definiert. Mit einer Weisslichtquelle wären daher theoretisch auch räumliche Auflösugen im sub-mikrometer Bereich möglich. Der dritte Teil dieser Arbeit beschreibt das Prinzip der neuen Methode und stellt die Ergebnisse aus ersten Validierungtests vor.

Abstract

The work reported in this thesis was carried out at the Institute of Fluid Dynamics, ETH Zurich, between 2002 and 2006. The work was mainly funded by ALSTOM Power Switzerland as a part of the Center of Energy Conversion - CEC co-operation between ETH and ALSTOM.

This thesis introduces two novel methods for sensing applications in low coherence interferometry. For the first time under operating conditions the tip clearance of an early stage of a power plant gas turbine has been measured in detail. On the other hand a new technique of laser velocimetry has been developed, allowing contactless boundary layer measurements over moving surfaces.

The "Tip Clearance Probe" was the initial project. This measuring system has been developed to obtain temporally resolved tip clearance data from early stages of gas turbines. The working principle relies on the interference between backreflected light from the blade tips during the blade passage time and a frequency shifted reference. Common tip clearance sensors either do not have the temporal resolution or an adequate measurement range or they cannot withstand the high temperature loads. The low coherence interferometry technique adapted to tip clearance sensing allows to measure with absolute spatial accuracy of tens of microns. The probe can hence be mounted in a cooled recess without compromising accuracy. A prototype of the system, an all-fiber assembly, has been successfully applied to a laboratory cold-gas turbine and to the first stage behind the combustor of a large-scale power generation gas turbine (GT26-ALSTOM). The second part of this thesis outlines the principle of this sensor and reports on the turbine measurements.

The novel "Self-Referencing Boundary Layer Profiler" combines flow velocimetry measurements with the spatial high resolving qualities of low coherence interferometry. The new approach is that both the object to be measured and an optical reference are outside of the interferometer, i.e., they are self-referenced to each other. Thus, the technique is applicable to contactless measurements of near surface flows, even if the surface moves irregularly. The measurement location is always selected based on its distance to an reference object. The distance can be adjusted without moving optical parts in the sensor head, but by varying the path lengths in the interferometer arms. The absolute accuracy of the measurement location and the spatial resolution depend on the properties of the low coherence light source, with typical values of tens of microns. The working principle of this new technique and proof-of-principle tests are described in the third part of this thesis.

Part I

Theory

Introduction

This part of the thesis is intended to give a brief overview about relevant fields of optics, lasers, interferometry and laser velocimetry. Together with a number of historical facts only basic background knowledge is presented, not claiming completeness. For further information one can follow the given references used as source of this short summary.

The term *optics* originates form the greek phrase *téchnē optikē*, respectively from the latin phrase *ars optica*, both meaning the lore relevant for vision (Kaliske, 1996). Thereby, this stands for the science of light, with its origination, propagation and perception. In the sense of natural sciences this means the physics of electromagnetic radiation, wherein the visible light is only a small part. Electromagnetic waves as a major part of todays physics exhibit a variety of exciting phenomena, which are often simply fascinating for everybody.

Historical deliverances about optics go back to first great civilizations, such as the ancient Babylon or Egypt. So, empirical knowledge about light reflection and the straight propagation of light was already existent. Nevertheless, light had almost everywhere some form of spiritual character. Between 500 B.C. and 200 the Greeks *Empedokles, Plato, Euklid, Aristoteles, Archimedes, Claudius* and *Ptolemaus* have been involved in the development of knowledge about light in the scientific sense. The Greek already could mathematically describe light reflection and refraction. It was also known that human vision is only possible when something is illuminated by light. Unfortunately, due to the fact that *Aristoteles* disliked experiments, the Greek and also later theories were partly incorrect, simply because sometimes they were not verified at all.

After the Hellenistic civilization many of their scientific writings has been destroyed in wars or they got lost. Around the year 1000, *Alhazen Mohammed Ibn el Heitam*, a persian scientist, wrote an opus *"Kitab-al-Manazir" (treasure of optics)*. His theories were based on the old Greek papers. In the Europe of the Middle Age most scientists shared *Aristoteles* attitudes. First with *Robert Grosseteste (1168/75-1253)* and mainly with his student *Roger Bacon (1214-1294)* experiment and theory together were seen as the way of science. With the translation of the theories of *Ptolemaus* and *Ibn el Heitam* into Latin by the end of the 12th century, the knowledge of optics in Europe slowly increased.

From then on many scientists and also painters became aware of novel optical laws and they developed their own theories, e.g., *Isaac Newton (1643-1727)* and *Leonardo da Vinci (1452-1519)*. A real breakthrough was achieved in 1817 by *Thomas Young*, since he first saw light as a transversal wave. Independently, *Augustin Fresnel* developed similar theories around the same time. In 1845 *Micheal Faraday (1791-1867)* found a first indication for a relationship between light and electromagnetism. He

showed experimentally that the polarization of light can be rotated by a magnetic field. Following this suggestion, *James Clerk Maxwell (1831-1879)* developed the theory of electromagnetic waves, which up to today is mainly used to describe the behavior of light. Nevertheless, in 1900 *Max Planck (1858-1947)* opened the book to the quantum mechanics and in turn also the development of lasers (light amplification by stimulated emission) in the mid 1950's.

Today, scientists are still actively conducting research in the field of light, e.g., quantum optics and non-classical light. So, for thousands of years light has fascinated many researchers and everybody else alike, and for sure it will continue to do so.

1 Fundamentals of Lasers and Optics

The description of electromagnetic waves presented in this thesis mainly follows the book *"Laser Doppler and Phase Doppler Measurement Techniques."*(Albrecht et al., 2003). For consistency the given equations for electromagnetic waves follow their nomenclature. Only differing references are explicitly cited.

1.1 Electromagnetic Waves

1.1.1 Mathematical Description

Light propagation can be described by the theory of electromagnetic fields, which is based on Maxwell's equations. For a harmonic oscillation, Maxwell's equations can be simplified by using the complex form (denoted through underlines)

$$\mathrm{curl}\underline{\mathrm{H}} = \underline{\mathrm{S}} + \mathrm{j}\omega\underline{\mathrm{D}}, \quad \mathrm{curl}\underline{\mathrm{E}} = -\mathrm{j}\omega\underline{\mathrm{B}} \tag{1.1a}$$

$$\mathrm{div}\underline{\mathrm{D}} = \rho_c\,, \quad \mathrm{div}\underline{\mathrm{B}} = 0 \tag{1.1b}$$

$$\underline{\mathrm{S}} = \varepsilon\underline{\mathrm{E}}\,, \quad \underline{\mathrm{D}} = \kappa\underline{\mathrm{E}}\,, \quad \underline{\mathrm{B}} = \mu\underline{\mathrm{H}} \tag{1.1c}$$

with $\underline{\mathrm{H}}$ as the magnetic field strength, $\underline{\mathrm{S}}$ as the current density, ω as the angular frequency, $\underline{\mathrm{D}}$ as the electric displacement, $\underline{\mathrm{E}}$ as electric field strength, $\underline{\mathrm{B}}$ as the magnetic induction and ρ_c as the charge density. The material properties are taken into account through the material constants ε, κ and μ, which represent the electric permittivity, the electrical conductivity and the magnetic permeability.

For a charge-free space ($\rho_c = 0$), these equations yield to two identical partial differential equations for the field parameters $\underline{\mathrm{E}}$ and $\underline{\mathrm{H}}$, the electric and magnetic field strengths

$$\nabla^2\underline{\mathrm{E}} + \underline{k}^2\underline{\mathrm{E}} = 0 \tag{1.2a}$$

$$\nabla^2\underline{\mathrm{H}} + \underline{k}^2\underline{\mathrm{H}} = 0 \tag{1.2b}$$

Any solution of these two equations with k as the wavenumber can be interpreted as a wave, which might be the reason why they are more commonly known as the wave equations for an electromagnetic field. The wavenumber k is based on the dispersion relation

$$\underline{k} = \sqrt{\varepsilon\mu\omega^2 - \mathrm{j}\omega\kappa\mu} = \omega\sqrt{\underline{\varepsilon}\mu} \tag{1.3}$$

which describes the relation between the frequency of the wave and the material properties.

The propagation speed of an electromagnetic wave, known as the speed of light, is also given by the properties of the medium in which the wave propagates

$$c = \frac{1}{\sqrt{\varepsilon\mu}} = \frac{c_0}{\sqrt{\varepsilon_r\mu_r}} = \frac{c_0}{n} \tag{1.4}$$

with n as the index of refraction and c_0 as the speed of light in vacuum

$$c_0 = \frac{1}{\sqrt{\varepsilon_0\mu_0}} = 299,792,458\ ms^{-1} \tag{1.5}$$

The refractive index n itself depends on the frequency (wavelength) of the electromagnetic wave, as well as on the pressure and temperature of the propagation medium.

Homogeneous Plane Waves

A simple solution of the wave equations can be given for a non-conducting medium ($\kappa = 0$). With a wave described by a wave vector

$$\mathbf{k} = k\mathbf{e}_k = \frac{\omega}{c}\mathbf{e}_k = \frac{2\pi}{\lambda}\mathbf{e}_k \tag{1.6}$$

and assuming a sinusoidal wave behavior the Eqs. 1.2 can be transformed into the solutions for the field strengths

$$\underline{\mathrm{E}} = \mathrm{E}_0 \exp\left[\mathrm{j}\left(\omega t - kz\right)\right], \quad \underline{\mathrm{H}} = \mathrm{H}_0 \exp\left[\mathrm{j}\left(\omega t - kz\right)\right] \tag{1.7}$$

here with z as the propagation direction. The energy density is then given by

$$w = \frac{1}{2}\left(\mathbf{E}\cdot\mathbf{D} + \mathbf{H}\cdot\mathbf{B}\right) \tag{1.8}$$

and expresses the energy in an electrical field. For a homogeneous plane wave this equation can be further transformed to

$$w = \frac{1}{2}\left(\varepsilon E^2 + \mu H^2\right), \quad E = |\underline{\mathrm{E}}|, \quad H = |\underline{\mathrm{H}}| \tag{1.9}$$

In general the electric and magnetic field strengths are coupled and they contain the same amount of energy. Therefore, it is sufficient to express the energy density with the electric field only

$$w = \varepsilon E^2 \tag{1.10}$$

The Poynting vector *(after John Henry Poynting 1852-1914)*

$$\mathbf{P} = \mathbf{E} \times \mathbf{H} \tag{1.11}$$

describes the energy flux in an electromagnetic field. With the preceding simplifications the Poynting vector for a plane wave can be written as

$$|\mathbf{P}| = cw = c\varepsilon E^2 \tag{1.12}$$

1.1.2 Light Polarization

Light emanating from a source like the sun or a light bulb vibrates in all directions perpendicular to the direction of propagation and is thus called unpolarized. If instead, the light wave vibrates in a particular direction at a specific point in the propagation path the light is called polarized.

A homogeneous plane wave propagating in the z direction can be modeled as the sum of two independent partial waves with orthogonal field components (x,y)

$$\underline{\mathrm{E}}(t,z) = \mathbf{e}_x \underline{E}_x(t,z) + \mathbf{e}_y \underline{E}_y(t,z) \tag{1.13a}$$

$$\underline{E}_x = E_{0x} \exp\left[\mathrm{j}\left(\omega t - kz + \varphi_x\right)\right] \tag{1.13b}$$

$$\underline{E}_y = E_{0y} \exp\left[\mathrm{j}\left(\omega t - kz + \varphi_y\right)\right] \tag{1.13c}$$

where both components are perpendicular to the propagation direction $\mathbf{k} = k\mathbf{e}_z$. Furthermore, these two field components can have a relative phase shift $\Delta\varphi = \varphi_x - \varphi_y$. Depending on the amplitudes of the partial waves and their relative phase shift, linear, right or left circular, as well as elliptical polarized light can occur.

1.1.3 Mixing of Electromagnetic Waves

If more than one electromagnetic wave hits a detector surface, optical mixing occurs. The electric field strength at a detector then becomes the sum of all impinging intensities. Consider two electromagnetic waves impinging on a detector surface with its $x-y$ plane normal to both wave directions. What the detector is exposed is

$$\underline{\mathrm{E}} = \sum \underline{\mathrm{E}}_i = \sum \left(\mathbf{e}_x \underline{E}_{xi} + \mathbf{e}_y \underline{E}_{yi}\right) \tag{1.14a}$$

$$\underline{E}_{xi,yi} = E_{xi,yi} \exp\left[\mathrm{j}\left(\omega_i t - k_i z + \varphi_{xi,yi}\right)\right] \tag{1.14b}$$

1.1.4 Laser Light

Monochromatic Light

Monochromatic light is theoretically light consisting of just one wavelength. No light is absolutely single frequency since it will have some bandwidth Δf. Lasers provide some of the narrowest bandwidths which can be achieved.

Non-Monochromatic Light

Generally speaking non-monochromatic light is found everywhere, since also lasers can not provide single frequency light. In technical terms non-monochromatic light means all light except the narrow bandwidth laser light. A number of natural and technical light sources with their bandwidths are listed in the following table.

light source	white light	SLD	spectral lamp	GaAlAs laser	HeNe laser
frequency bandwidth	$\approx$ 200 THz	$\approx$ 6 THz	1.5 THz	2 MHz	150 kHz
coherence length	$\approx$ 1 μm	$\approx$ 50 μm	20 cm	150 m	2 km

Table 1.1: Spectral bandwidths and coherence lengths of various light sources.

The distribution of the light power over the wavelength must be considered for the choice of detector material, see Chapt. 1.2.1. For that, commonly the power spectral density $\mathscr{P}(f)$ or the energy spectral density $\mathscr{E}(f)$ of a light source is known. They can be defined as

$$\mathscr{P}(f) \hat{=} \int_{-\infty}^{\infty} \mathscr{A}(\tau) \exp\left[j\,(2\pi f \tau)\right] d\tau \tag{1.15a}$$

$$\mathscr{E}(f) \hat{=} |\mathscr{F}(f)|^2 \tag{1.15b}$$

with $\mathscr{F}(f)$ as the Fourier transformation and $\mathscr{A}(\tau)$ as the autocorrelation[1] of $E(t,z)$. The fluctuations in the electric field of non-monochromatic light can then described as an analytic signal (only positive frequencies allowed)[2]

$$\underline{E_a}(t,z) = 2 \int_0^{\infty} \sqrt{\mathscr{E}(f)} \exp\left[\mathrm{j}\,(2\pi f(t - z/c) + \varphi)\right] df \tag{1.16}$$

[1] For the definition of autocorrelation see Chapt. Correlation Method 3.3.2.

[2] The factor two originates from the negative frequency components, which double the strength of the positive frequencies (Goodman, 1988).

Optical Coherence Temporal/Spatial[3]

In general one has to differentiate between two types of coherence, *temporal coherence* and *spatial coherence*. Temporal coherence means the ability of a light beam to interfere (constructive optical mixing) with a delayed, but spatially not shifted, version of itself. Spatial coherence, on the other hand, means the ability of a light beam to interfere with a spatially shifted, but not delayed, version of itself. Allowing temporal and spatially shifting together leads to the concept of mutual coherence.

A measure of coherence is provided by the definitions of the *complex degree of coherence* $\gamma(\tau)$, which represents a normalized version of the *self coherence function*, which in turn is the autocorrelation $\mathscr{A}(\tau)$ of the analytic signal $\underline{E_a}(t,z)$

$$\gamma(\tau) = \frac{\mathscr{A}(\tau)}{\mathscr{A}(0)} \tag{1.17}$$

According to Mandel (1959) the *coherence time* τ_c can be defined as

$$\tau_c \hat{=} \int_{-\infty}^{\infty} |\gamma(\tau)|^2 \, d\tau \tag{1.18}$$

Furthermore, the *coherence length* l_c is the distance which the light propagates within the coherence time

$$l_c = c\tau_c \tag{1.19}$$

First, consider a ultrashort laser pulse, for example, $\tau = 0.1\bar{6}$ ps (FWHM). The phase remains constant over the Gaussian shaped pulse, see upper left panel of Fig. 1.1. The complex degree of coherence of the pulse is shown in the right panel. According to the definition Eq. 1.18, the coherence time can be determined as $\tau_c = \sqrt{\frac{2ln2}{\pi}} \cdot \tau = 0.11$ ps.

Next, consider a continuous signal of a broadband light source. Unlike one might expect, the coherence length of the signal is not infinite. To explain this, one can focus on the special relationship between the autocorrelation function and the power spectral density, known as the *Wiener-Khinchin theorem*. Here, the autocorrelation function and power spectral density forms a Fourier transform pair

$$\mathscr{P}(f) = \int_{-\infty}^{\infty} \mathscr{A}(\tau) \exp\left[j\,(2\pi f\tau)\right] d\tau \tag{1.20a}$$

$$\mathscr{A}(\tau) = \int_{-\infty}^{\infty} \mathscr{P}(f) \exp\left[-j\,(2\pi f\tau)\right] df \tag{1.20b}$$

[3] Goodman (1988)

Corresponding to Goodman (1988) the complex degree of coherence in terms of power spectral density can then be expressed as

$$\gamma(\tau) = \int_0^\infty \hat{\mathscr{P}}(f) \exp\left[-j\,(2\pi f \tau)\right] df \tag{1.21a}$$

$$with \int_0^\infty \hat{\mathscr{P}}(f) df = 1 \tag{1.21b}$$

$\hat{\mathscr{P}}(f)$ is the normalized power spectral density, see lower left panel Fig. 1.1.

With Eq. 1.18 the coherence time of a broadband light source can now be expressed as a function of the frequency bandwidth Δf

$$\tau_c = \frac{f_{\mathscr{P}}}{\Delta f} \tag{1.22}$$

with $f_{\mathscr{P}}$ as a form factor of the spectral shape of the power density spectrum and Δf as the FWHM bandwidth (half power bandwidth). In particular, $f_{\mathscr{P}}$ is 1 for a rectangular, 0.318 for a *Lorenzian* and 0.664 for a *Gaussian* spectrum.[4]

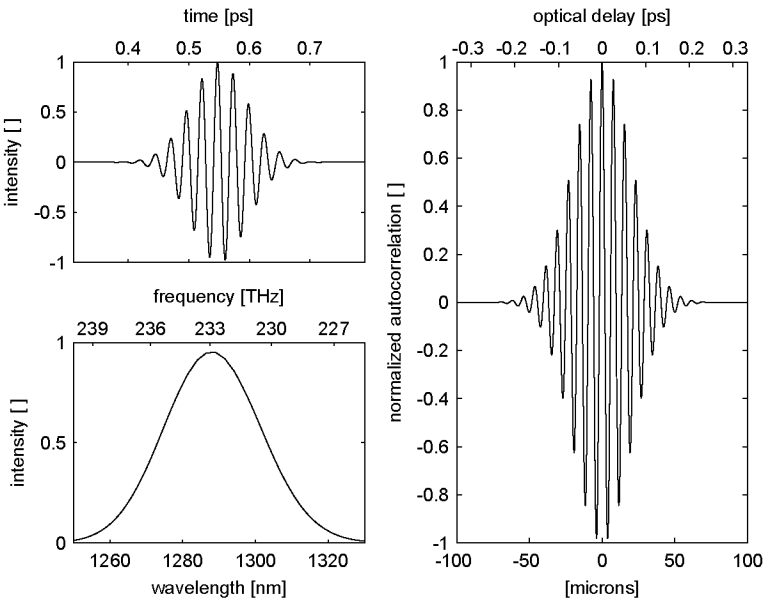

Fig. 1.1: Laser pulse, complex degree of coherence and power spectral density.[5]

[4] Please note: the factor $f_{\mathscr{P}}$ given here is valid for energy fluctuations. For intensity fluctuations as measured by photoreceivers the square of $f_{\mathscr{P}}$ has to be considered.

[5] For visualization the wavelength in the figure is scale up by a factor of 6. The duration of the pulse was chosen such that the power spectral density is equivalent to that of Superlum SLD-HP-56-HP (Fig. 1.4).

For spatial coherence consider a non-monochromatic point source of zero diameter. It emits temporal low coherence light, which on the other hand is highly spatially coherent. The light from a collection of incoherent point-sources instead would have lower spatial coherence. If multiple point sources are coherent with each other, e.g., multiple slits in a Young's slit experiment, there is no loss of spatial coherence. Spatial coherence can be increased with a spatial filter, i.e., a very small pinhole. The spatial coherence of light will also increase as it travels away from the source as the source appears smaller (more pointlike) and the waves become more like a plane wave.

1.2 Optical Components

1.2.1 Photodetectors

Fluctuations of the energy density of light waves cannot be measured directly. Usually the photodetectors used for light detection do not have such high frequency resolution because of the inertia of electron emission. Thus, a photodetector shows an intensity fluctuation I as temporal average of the Poynting vector (Eq. 1.12). In complex notation this leads to a simple mathematical representation for the electromagnetic intensity

$$I = \frac{1}{T}\int_T |\mathrm{P}|\,\mathrm{dt} = \frac{c\varepsilon}{2}\underline{\mathrm{E}}_\perp \cdot \underline{\mathrm{E}}^*_\perp \tag{1.23}$$

The power detected on a photodiode includes furthermore the integration of Eq. 1.23 over the sensitive surface of the detector

$$P_p = \iint_A I\,\mathrm{dA} \tag{1.24}$$

The perpendicular symbols in Eq. 1.23 indicate that only components perpendicular to the detector's surface directly contribute to the electron emission. Other vector components result in detector losses. The output of electric current is directly proportional to the detected power

$$i_p = G\,\frac{q\eta_q}{hf}\,P_p \tag{1.25}$$

with q as elemental charge, η_q as the quantum efficiency (a factor which considers the detector's material properties), h as the Planck constant *(after Max Planck 1858-1947)* and f as the light frequency. In addition, the generated signal in a photodetector is amplified, here accounted for by gain factor G.

Due to the time averaging behavior of the photodetector, all frequencies above a certain cut-off frequency f_c are represented as a DC current signal component.

Therefore the output current of a detector can be described by the sum of a DC component and further AC parts

$$i_p = i_{DC} + i_{AC} \cos(\omega t + \varphi) = i_{DC} [1 + m \cos(\omega t + \varphi)] \tag{1.26a}$$

$$m = \frac{i_{AC}}{i_{DC}} \tag{1.26b}$$

with m as the so-called modulation depth or visibility.

Technical Characteristics [6]

Spectral Responsivity $\mathbf{R}_\lambda$ The responsivity of a photodiode is a measure of the sensitivity to light and it is defined as the ratio of the photocurrent i_p to the received light power P_p at a given wavelength:

$$R_\lambda = \frac{i_p}{P_p} \tag{1.27}$$

In other words, it is a measure of the effectiveness of the conversion of the light power into electrical current, see Fig. 9.1. It varies with the wavelength of the incident light as well as with the applied reverse bias and the temperature.

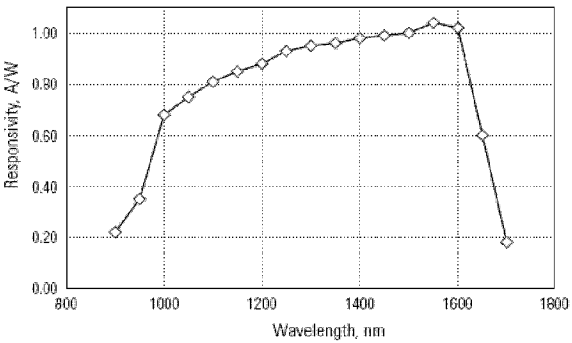

Fig. 1.2: Responsivity of a photoreceiver - Newport model 1811.

[6] UDT Sensors Inc. (2006)

Dark Current The current-voltage characteristic of a photodiode with no incident light is similar to a rectifying diode. When the photodiode is forward biased, there is an exponential increase in the current. When a reverse bias is applied, a small reverse saturation current appears. The dark current is related to this as

$$i_d = i_{SAT} \left(e^{\frac{qV_A}{k_B T}} - 1 \right) \tag{1.28}$$

with i_{SAT} as the reverse saturation current, V_A as the applied bias voltage, k_B as the Boltzmann constant *(after Ludwig Eduard Boltzmann 1844-1906)* and $T[K]$ as the absolute temperature.

Shot Noise Shot noise is related to the statistical fluctuations in both the photocurrent and the dark current. The magnitude of the shot noise is expressed as the root mean square (rms) noise current

$$i_{sn} = \sqrt{2q \left(i_p + i_d \right) \Delta f} \tag{1.29}$$

with Δf as the measurement bandwidth. Shot noise is the dominating source when operating in photoconductive (biased) mode.

Johnson-Nyquist Noise The shunt resistance in a photodetector displays a Johnson-Nyquist noise *(after John Bertrand Johnson 1887-1970 and Harry Nyquist 1889-1976)*. This is due to the thermal generation of carriers. The magnitude of this generated current noise is

$$i_{jn} = \sqrt{\frac{4k_B T \Delta f}{R_{SH}}} \tag{1.30}$$

with R_{SH} as the shunt resistance of the photodiode. This type of noise is the dominant current noise in photovoltaic (unbiased) operation mode.

Noise Equivalent Power (NEP) Noise Equivalent Power is the amount of incident light power on a photodetector, which generates a photocurrent equal to the noise current

$$NEP = \frac{\sqrt{i_{sn}^2 + i_{jn}^2}}{R_\lambda} \tag{1.31}$$

In other words the NEP (in $W/\sqrt{Hz}$) represents the minimum light power which can be detected with a photodiode at a given frequency bandwidth.

1.2.2 Optical Fibers [7]

In the 1840's, the Swiss physicist *Daniel Collodon* and the French physicist J*Jacques Babinet* showed that light can be guided along jets of water. In 1854, *John Tyndall*, a British physicist, popularized light guiding in a demonstration, guiding light in a jet of water flowing from a tank to another. As water poured out through the spout of the first container, Tyndall directed a beam of sunlight at the path of the water. Due to the effect called internal reflection, the light seen by the audience followed a zigzag path inside the curved path of the water. By the turn of the century, inventors realized that bent quartz rods could carry light, and patented them as dental illuminators.

Heinrich Lamm as medical student in Munich demonstrated image transmission through a bundle of optical fibers. His goal was to look inside inaccessible parts of the body. In a 1930 paper he reported on transmitting a image of a light bulb filament through a short bundle. A crucial innovation was made by *Abraham van Heel* in 1954. He first covered a bare fiber with a transparent cladding of a lower refractive index. This protected the total reflection surface from contamination and greatly reduced crosstalk between fibers. Since then fiber optic research has led to a dramatic improvement in light guiding performance and fibers are used today in a wide field of applications, especially in telecommunication and medicine.

Basically, optical fibers are classified into two types, single mode fibers and multimode fibers. Furthermore, fibers may be categorized as step-index or graded-index fibers.

Multimode Step-Index Fiber

Fig. 1.3 shows the principle of total internal reflection in a multimode step-index fiber. Because the index of refraction of the fiber core is higher than that of the cladding, light within the numerical aperture (NA) can enter the fiber and is then guided along. The numerical aperture of a step-index fiber can be described as

$$NA = n_0 \sin\theta_A = n_0\sqrt{n_1^2 - n_2^2} \tag{1.32}$$

with n_1 and n_2 as the refractive indicies of the fiber's core and cladding media and n_0 as the refractive index of the surrounding medium, which normally is air with $n_0 \approx 1$. For a multimode fiber, different light modes can be transmitted. The different modes enter the fiber at different angles and then each mode for itself bounces back and forth by total internal reflection (see Fig. 1.3). It can be seen that the different modes travel different distances inside the fiber, causing the two modes to arrive at separate times. This disparity between arrival times of the different light rays is known as dispersion, and the result is a distorted signal at the receiving end. This is especially important for interferometry applications, see Chapt. 2.2.2.

[7] Hecht (2006) and Force Inc. (2006).

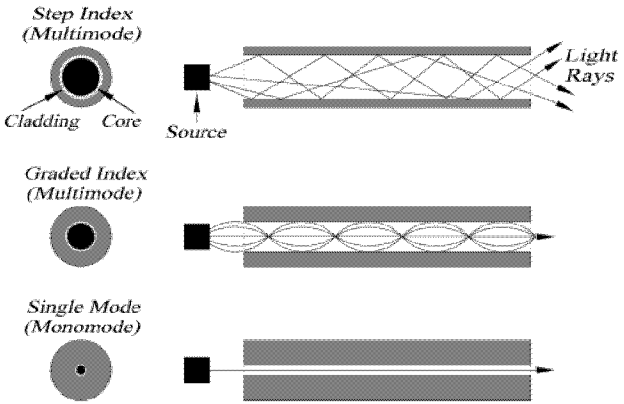

Fig. 1.3: Types of optical fibers.

Multimode Graded-Index Fiber

Graded-index refers to the fact that the refractive index of the core gradually decreases from the center of the core

$$NA(r) = n_0 \sin\theta_A = \sqrt{n_1^2(r) - n_2^2} \tag{1.33}$$

As Fig. 1.3 shows, the light rays no longer follow straight lines. Instead they follow a serpentine path being gradually bent back towards the center by the continuously varying refractive index. This reduces the arrival time disparity because all modes arrive at about the same time. The modes traveling in a straight line are in a region of higher refractive index, so they travel more slowly than the serpentine modes. These travel farther but faster in the lower refractive index of the outer core region.

Singlemode Fiber

As the core radius of a fiber decreases, the number of possible propagation modes decreases, too (see Fig. 1.3). With a core radius of about 3..10 μm, singlemode fibers allow only one mode to propagate. Dependent on the wavelength, the number of modes carried is described by the so called V-parameter

$$V = \frac{2\pi\, r_{core}}{\lambda} NA \tag{1.34}$$

The number of modes which can enter the fiber is approximately V^2. The smaller core diameter of singlemode fibers makes coupling light into the core more diffi-

cult. Similarly, the tolerances for singlemode connectors and splices are much more demanding.

An additional important variety of singlemode fiber is the polarization maintaining (PM) fiber. The PM fiber is designed to guide only one polarization of the input light. Next the core, there are two additional filaments called stress rods. These stress rods create stress in the core of the fiber such that the transmission of only one polarization plane of light is favored.

1.2.3 Optical Gratings and Bragg Cells [8]

Optical gratings and Bragg cells are often used as beamsplitters, modulators or frequency shifters. In laser Doppler systems frequency shifting gives the possibility to determine the direction of the flow velocity. Kerr cells or Pockels cells are also feasible as frequency shifting devices, but due to the limited quality, frequency variations and low frequency shift, they have not become common in laser Doppler applications.

Diffraction Grating

For diffraction through a slit the intensity of the diffracted light can be expressed as

$$\frac{I_p}{I_0} = \frac{\sin^2\left(\frac{\pi b}{2\lambda}\left(\sin\beta_p - \sin\alpha\right)\right)}{\left(\frac{\pi b}{2\lambda}\left(\sin\beta_p - \sin\alpha\right)\right)^2} \tag{1.35a}$$

$$\sin\beta_p = \sin\alpha \pm \frac{p\lambda}{b}, \quad p = 0, 1, 2... \tag{1.35b}$$

where α is the incidence angle, β_p the diffraction angle of order p and b the grating width. The assumptions are that the source and the receiver are far away from the grating, the grating length l is much larger than its width b, that b is larger than two times the wavelength $b > 2\lambda$ and the amplitude or phase changes across the grating are sinusoidal. The incidence angle here changes only the position of the intensity maximum.

If the grating is moving perpendicular to the incident light ($\alpha = 0$), the diffracted light experiences a Doppler frequency shift, see Chapt. 3.2.1.

[8] AA-Opto-Eelectronic (2003).

Bragg Cells

A Bragg cell creates a phase grating with acoustically generated pressure waves within a crystal. A so-called quality factor Q defines the interaction regime between the acoustic and light waves (AA-Opto-Eelectronic, 2003)

$$Q = \frac{2\pi\lambda l}{n\Lambda^2} \tag{1.36}$$

with λ as the light wavelength, Λ as the acoustic wavelength, n as the refractive index of the crystal and l as the length over which the light wave interacts with the acoustic wave. For $Q << 1$ and $Q >> 1$ two interaction regimes can be distinguished.

Raman-Nath regime For $Q << 1$ the light roughly normal to the acoustic waves is diffracted into several orders $(..., -2, -1, 0, 1, 2, ...)$ with an intensity given by the Bessel function.[9]

Bragg regime For $Q >> 1$ the light has to be at a certain incidence angle. Only then the light is refracted optimally at its 1st order with twice the incidence angle, the other orders are annihilated by destructive interference.

1.2.4 Superluminescent Light Emitting Diodes (SLD's)

The special property of superluminescent diodes (SLD's)[10] is the combination of laser-diode-like output power with a broadband optical spectrum. The large bandwidth translates into a short coherence length allowing SLD's to be used as low coherence interferometry light sources (see Chapt. 2.2). The small form factor and user friendly operation make them advantageous. High power SLD's have first been developed in 1989 by Gerard A. Alphonse, Alphonse et al. (1988).

SLD's are based on a p-n-junction embedded in an optical waveguide. When biased electrically in the forward direction they show optical gain and generate amplified spontaneous emission over a wide range of wavelengths. They are designed to have high single pass amplification, but unlike laser diodes, the feedback is insufficient to perform lasing action. A rejection of the cavity modes is typically achieved by tilting the waveguide with respect to the end facets and with anti-reflection coatings at the facets. Thus a smooth broadband spectrum, which is temporally incoherent,

[9] Chandrasekhara Venkata (C.V.) Raman (1888-1970). In 1930 Raman was awarded the Nobel prize in physics for his 1928 discovery of the Raman Effect, which demonstrates that the energy of a photon can undergo partial transformation within matter. In 1934-36, with his colleague Nagendra Nath, Raman proposed the Raman-Nath Theory on the diffraction of light by ultrasonic waves. He was director of the Indian Institute of Science and founded the Indian Academy of Sciences in 1934 and the Raman Research Institute in 1948 (Coutsoukis, 2006).

[10] Please note: frequently used acronyms for the superluminescent diode are SLD and alternative SLED. However, SLED is not recommended, because it is more often used for surface-emitting LED, i.e., with a totally different meaning.

can be generated. The small emission area of the SLD leads to a high spatial coherence, which facilitates the light coupling into optical singlemode fibers. Typically the coupling efficiency is better than 50 % (Böhm & Overbeck, 2005). The optical output power out of a singlemode fiber ranges from 1 to 30 mW depending on the center wavelength.

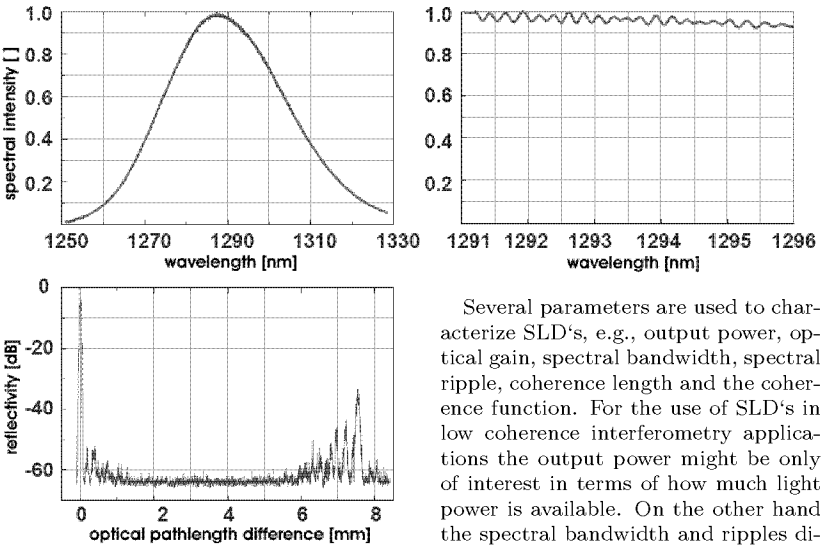

Fig. 1.4: Performance of SLD-HP-56-HP (Superlum Diodes Ltd, 2005).

Several parameters are used to characterize SLD's, e.g., output power, optical gain, spectral bandwidth, spectral ripple, coherence length and the coherence function. For the use of SLD's in low coherence interferometry applications the output power might be only of interest in terms of how much light power is available. On the other hand the spectral bandwidth and ripples directly affect the coherence behavior of the light, which in turn defines the performance of a low coherence interferometer. Eq. 1.22 describes in simple terms the relations between spectral bandwidth and coherence length.

In addition, the coherence function expresses the reflectivity (intensity) versus the difference in optical path length. Here the spectral ripples result in sub-peaks at an optical path length difference which is equal to $2n_{eff}L$, with n_{eff} as the effective refractive index of an optical mode and L as the active length of the SLD. The intensity of secondary coherence sub-peaks is determined by the integral value of the spectral modulation across the entire spectrum (Inphenix, Inc, 2004). In general, secondary coherence sub-peaks should be avoided or as low as possible.

2 Interferometry

Interferometry relies on the principles of interference to determine properties of waves, their sources, or the wave propagation medium. Interference is understood as the superposition of two or more waves. When waves moving along their direction of propagation, either from one source using different paths or from different sources, reach the same point in space at the same time, interference occurs. If the waves arrive in-phase (the crests arrive together), constructive interference occurs. The combined crest is an enhanced version of the one from the individual wave. When they arrive out-of-phase (the crest from one wave and a trough from another), destructive interference cancels the wave motion. Please note: the energy of the wave is not lost, it moves to areas of constructive interference.

Acoustic interferometry has been applied to study the velocity of sound in a fluid. Radio astronomers use interferometry to obtain accurate measurements of the position and properties of stellar radio sources. Optical interferometry is widely used to observe objects without touching or otherwise disturbing them. Interpreting the fringes reveals information about optical surfaces, the precise distance between the source and the observer, spectral properties of light, or the visualization of processes such as crystal growth, combustion, diffusion or shock wave motion.

The most striking examples of interference occur in visible light. Interference of two or more light waves appears as bright and dark bands called "fringes." Interference of light waves was first described in 1801 by *Thomas Young (1773-1829)* when he presented information supporting the wave theory of light. The observation and explanation of interference fringes in general dates back to *Robert Hooke (1635-1703)* and *Isaac Newton (1643-1727)*. Nevertheless the invention of interferometry is widely attributed to the American physicist *Albert Abraham Michelson (1852-1931)*.

It is important to note that almost every observation of interference is time averaged. Thus, interfering waves must be coherent, i.e., they need to have a predictable phase relationship. Otherwise, for random phase changes between two waves, the interference signal is destroyed.

2.1 Michelson-Interferometer

A very common example of an interferometer is the Michelson (or Michelson-Morley) type *(after Albert Michelson (1852-1931) and Edward Williams Morley (1838-1923))*. The basic building blocks are a light source (or matter source), a detector, two mirrors and one semitransparent mirror (often called beamsplitter), arranged as shown in Fig. 2.1. There are two possible paths from the source to the detector. One

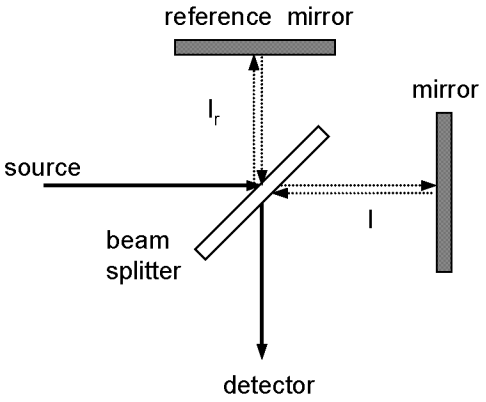

Fig. 2.1: Basic principle of a Michelson interferometer.

goes to the beamsplitter, over the top mirror straight back through beamsplitter to the detector. The other goes through the beamsplitter to the mirror on the right and then from the beamsplitter towards the detector. For this situation note that on the way back from the two mirrors there is also light which goes back to the source. This will always causes a loss of the initial power.

If the two paths differ by a whole number (including 0) of wavelengths, there is constructive interference and a strong signal at the detector. If they differ by a whole number and a half wavelengths (e.g., 0.5, 1.5, 2.5 ...) there is destructive interference and a weak signal. Due to this periodicity, measurements of absolute pathlength differences larger than a wavelength tend to be difficult, because one has to count the number of waves.

2.2 Low Coherence Interferometry (LCI)

Low coherence interferometry is a special kind of interferometry. Instead of strongly coherent monochromatic light, broadband or ultrashort short pulsed light with a short coherence length is used. Contrary to interferometry with monochromatic light, the short coherence length of broadband light defines an additional absolute reference. This means that interference between two waves is possible only if the pathlength difference is smaller than the coherence length. Thus, LCI has found a wide range of technical applications, i.e., in biomedical imaging or topographical surface analysis, and is today often known as optical coherence tomography (OCT).

In Sect. 1.1.4 it is shown that the coherence length of light is determined by its self coherence function, with in turn is an interferogram, see Fig. 2.3. It is also shown that low coherence light can be seen either as ultrashort pulsed monochromatic light

or equivalently as broadband light. For the latter there is a fixed mathematical relationship between the power spectral density and the self coherence function, which is known as the *Wiener-Khinchin* theorem. Physically, one might regard continuous emitted broadband light also as pulses, but instead of the light amplitude, its phase changes pulsewise by a random value. For a time averaged interferogram this means also loss of coherence.

2.2.1 Principle

As mentioned low coherence interferometry basically does not differ in the design of the optical components from a classical interferometer. Only the monochromatic and coherent light source is replaced by a light source with certain short coherent light pulses. Consider the upper mirror in Fig. 2.1 as a reference, where the distance $d_r = 2l_r$ to the beamsplitter is known. The right mirror instead is located at an unknown distance d. The reference mirror can be moved back or forth until interference occurs. Since interference can only be observed if the optical path length difference (twice the distance to the beamsplitter) of the reference and the second mirror is within the coherence length of the light source, the position of the second mirror is hence known by the position of the reference mirror (see Fig. 2.2)

$$d = d_r \tag{2.1a}$$

$$|(d - d_r)| = 2\,|(l - l_r)| \quad < \quad l_c \tag{2.1b}$$

Replacing the second mirror by an object to be investigated, gives rise to various LCI applications such as, for example surface profilometry.

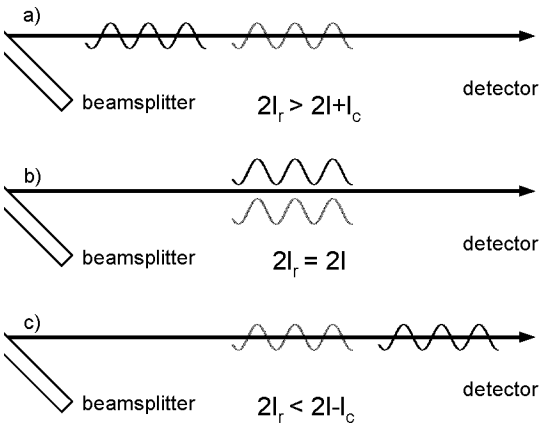

Fig. 2.2: Low coherence interferometry principle: a) path of reference wave (bold) too long c) path of reference wave to short b) pathlength difference of both waves is within the coherence length, i.e., interference occurs.

To make possible interference visible on the detector, one light beam in the interferometer can be shifted in its frequency. Following the optical wave mixing equations Eqs. 1.14 in Chapt. 1.1.3, the sum of two equal waves with the same phase, polarization, pathlength and propagation direction, but with a different amplitude and frequency can be expressed as

$$\underline{\mathrm{E}} = \underline{\mathrm{E}}_1 + \underline{\mathrm{E}}_2 = E_1 \exp\left[j\left(\omega_1 t - kz\right)\right] + E_2 \exp\left[j\left(\omega_2 t - kz\right)\right] \tag{2.2}$$

According to Eq. 1.23 the averaged intensity is then

$$I = \frac{c\varepsilon}{2}\underline{\mathrm{E}} \cdot \underline{\mathrm{E}}^* = \frac{c\varepsilon}{2}\left[E_1^2 + E_2^2 + 2E_1E_2\cos\left(\omega_2 t - \omega_1 t\right)\right] \tag{2.3}$$

This equation can be split into two parts, one corresponding to the DC term and one to the AC components of the intensity

$$I_{DC} = \frac{c\varepsilon}{2}\left(E_1^2 + E_2^2\right) \tag{2.4a}$$

$$I_{AC} = c\varepsilon E_1 E_2 \cos\left(\Delta\omega t\right) \tag{2.4b}$$

If the frequency difference $\Delta\omega$ of the AC part is within the detector's frequency bandwidth, the output current on the detector is similar to Eqs. 1.26

$$i_p = i_{DC}\left[1 + m\cos\left(\Delta\omega t\right)\right] \tag{2.5}$$

with $\Delta\omega$ as the frequency of the beat note representing an indicator for interference.

Thus, one can focus on the intensity of the beat note to recover the envelope of an interferogram. Delaying the reference reflection in an interferometer from $d_r < (d - l_c)$ to $d_r > (d + l_c)$, the beat note intensity can be recorded. As an example, Fig. 2.3 shows measured interferograms using a broadband light source with a nearly Gaussian shape (Superlum SLD-HP-56-HP, Fig. 1.4). The bold line represents the square of the self-coherence function out of Fig. 1.1, simulating a perfect Gaussian shape light source with the spectral width of SLD-HP-56-HP. The dotted line shows the interferogram measured with a freespace Michelson interferometer, which is slightly broader than the simulated data. The dashed line shows the data recovered with the fiberoptical interferometer used for this thesis, see Chapt. 5.1 and 8.2. It can be seen, that the measured data shows a coherence length which is by a factor of 4 larger than expected. One explanation for this might be multiple reflections within the interferometer, e.g., at each fiber connectors. This results in a number of light waves which are delayed to each other. If one assume that each multiple reflection is associate with loss of light power, the interferogram might be stretched as shown in Fig. 1.1. However, for the measurements with the fiberoptical setup, the larger coherence length needs to be considered.

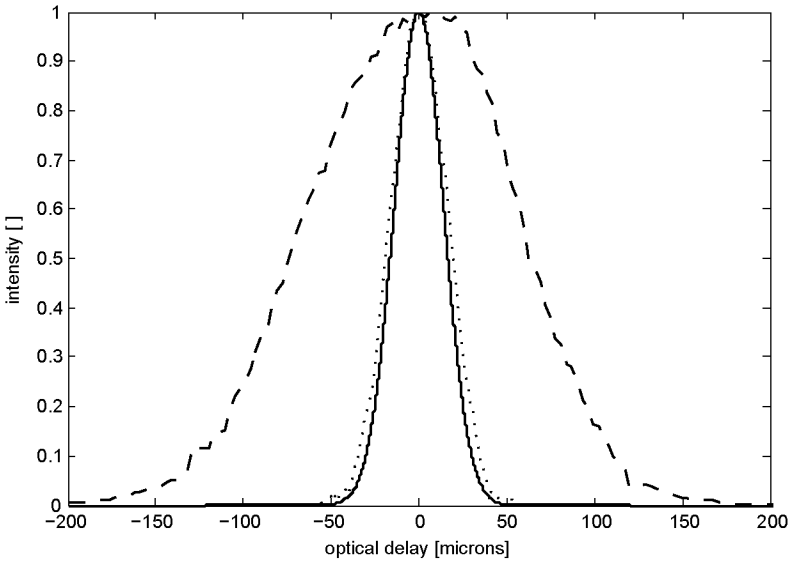

Fig. 2.3: Interferogram of Superlum SLD-HP-56-HP: bold line - simulated data (square of self coherence function, Fig. 1.1, dotted line - measurement with a freespace Michelson interferometer, dashed line - measurement with the fiberoptical setup Chapt. 5.1 and 8.2.

2.2.2 Low Coherence Interferometry Applications

Low coherence interferometry (LCI), low coherence reflectometry, optical coherence tomography (OCT) all refer to the same basic principle, an interferometer under low coherence illumination. A number of LCI systems have been researched and applied to different fields, in measuring electric or magnetic fields, pressure, acceleration, flows, etc.. To provide a small overview, three major fields of LCI are briefly described in the following.

Optical Coherence Tomography - OCT

Optical Coherence Tomography (OCT), first introduced by Huang et al. (1991), is a noninvasive imaging technique for cross-sectional sub-surface tissue imaging based on the principles of low coherence interferometry. It is one of the most prominent applications of LCI, revolutionizing the imaging technology of superficial tissue. A tissue structure can be imaged on micrometer scale in real time. The principle of OCT is analogous to that of ultrasound imaging, however, the contrast is derived from differences in optical rather than acoustic backscattering.

Optical Low Coherence Reflectometry - OLCR

Optical low coherence reflectometry (OLCR) is an interferometric technique that allows one to measure the amplitude and relative phase of reflected light. The technique was originally developed for reflection measurements in telecommunications devices with micrometer resolution. There, optical interfaces in complex structures can be precisely located and measured. The principle is based on coherent cross-correlation detection of light reflected from the sample. OLCR has also applications in medicine, e.g., for corneal thickness determination (Masters, 1999).

Distributed Laser-Doppler Velocimetry - DLDV

Distributed laser-Doppler velocimetry (DLDV) is a technique using low coherence interferometry for flow velocimetry. The technique was first presented by Gusmeroli & Martinelli (1991). It permits continuous interrogation of the flow velocity in any point belonging to a collimated laser beam. The technique can be seen as a special form of reference beam laser-Doppler velocimetry, see Chapt. 3.2.2.

DLDV uses low coherence light together with a Michelson interferometric configuration. The flow is illuminated by a collimated light beam. The position of the measurement volume can be chosen everywhere within the collimated beam, by setting the position of the reference within the interferometer. The size of the measurement volume depends on the beam diameter and the coherence length of the light source. Among the many particles crossing the sensing beam, only the particles within the coherent volume produce a interference signal. The flow velocity is determined by reference beam LDV frequency analysis.

3 Laser Velocimetry

3.1 Light Scattering of Small Particles

Optical flow velocimetry techniques are often based on the detection of the movement of small particles in the fluid, so-called seeding particles. The basic assumption is that the small seeding particles follow the fluid, thus representing the flow. However, this is also one major cause for measurement errors. The mass of the seeding involves an inertia, which leads to a delayed reaction of the particles in the flow field. Particularly for investigations in shock dynamics this is an essential issue. The smaller the particles the better is their ability to follow the flow, but also the lower is the intensity of the scattered light.

Generally speaking the size of seeding in gases is on the order of microns, which means it is comparable to optical wavelengths. Light scattering off such particles is characterized as Mie-scattering. Here the intensity of the backreflected light depends not only on the particle's shape, diameter and refractive index, but also and mostly on the observation angle. The phenomenon is well documented in literature, but also relative complex. A comprehensive summary, e.g., can be found in van de Hulst (1981). To give an example, Fig. 3.1 shows the general scattering behavior of micrometer sized particles. It can be seen, that the intensity of the forward

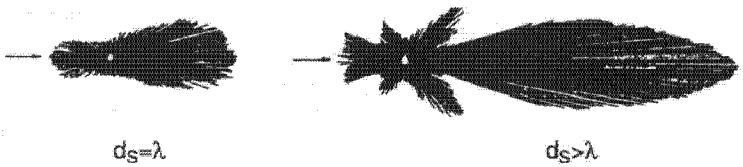

Fig. 3.1: Scattering behavior of small particles (Schodl, 1991).

scattered light is much larger than that of the backward scattered light. For a particle diameter $d_s > 2\lambda$, e.g., it is three orders of magnitude larger. Sidewards scattering strongly depends on the observation angle, and sometimes there is almost no scattering. Thus optical setups where the light source and the receiver are on a line (forward scattering) provide much better results. However, most times the optical access makes it impossible to build the system this way. Hence, the backward scattering setup is most popular for optical velocimetry techniques.

3.2 Laser-Doppler Systems

3.2.1 The Doppler Effect

The Doppler effect *(after Christian Andreas Doppler 1803-1853)*, is the apparent change in frequency or wavelength of a wave that is perceived by an observer moving relative to the source of the wave. For waves which do not require a medium (such as light waves) only the relative difference in velocity between the observer and the source needs to be considered.

It is important to realize that the frequency which the source emits does not actually change. Consider the following simple analogy. A person A throws one ball every second to a second person B. Assume that the balls travel with constant velocity. If A is stationary, B will receive one ball every second. However, if A is moving towards B, B will receive the balls more frequently, because there will be less spacing between the balls. The same is true if A is stationary and B is moving towards A. On the other hand the spacing between the balls increases, if A or B move away from each over. So it is actually the wavelength which is affected, and as a consequence, the perceived frequency too.

More generally the result in change of wavelength and frequency of electromagnetic waves can be expressed with

$$f \approx f_0 \left(1 - \frac{v_r}{c}\right) \tag{3.1}$$

with $|v_r| << c$, f as the light frequency detected by a receiver, f_0 as the frequency of the light source, c as the specific speed of light and v_r as the relative velocity between the source and the observer. The relative velocity is denoted positive, if the source and the observer are moving away from each other.

3.2.2 Laser-Doppler Velocimetry - LDV

Laser-Doppler velocimetry is a technique to obtain velocity data using the Doppler effect. In the field of flow analysis it is an indirect measurement technique, since it measures the velocity of inhomogeneities in the flow, so-called seeding particles.

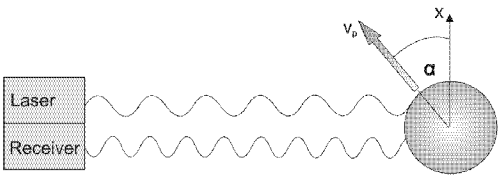

Fig. 3.2: Basic principle for LDA techniques (direct backward scattering).

The basic working principle is illustrated in Fig. 3.2. Due to that the particle acts both as a moving receiver and as a moving emitter of light, the frequency shift as a

result of the Doppler effect appears twice. The frequency shift as an equivalent of the particle velocity is then described by

$$\begin{aligned} f_{shift} &\approx f_0 \left(1 - \frac{v_p}{c}\right) - f_0 \\ &= -2 \cdot \frac{sin\alpha}{\lambda_0} \cdot v_p \end{aligned} \tag{3.2}$$

with $c = f \cdot \lambda$ and $|v_p| << c$ as the particle velocity. *Please note that the equation is only valid for LDA in direct backward scattering. The frequency shift will be positive for particles moving in laser direction.*

For typical flows the Doppler shift is in the order of $10^6 Hz$, which is very small compared to the frequencies of light of approximately $10^{14} Hz$. Thus a direct measurement of the Doppler shift tends to be impossible, since the cut-off frequencies of common photoreceivers are around $10^9 Hz$. However, e.g., with the help of an interferometer or the use of frequency dependent absorption cells the small Doppler shifts can be detected. Absorptions cells are often used for Doppler global velocimetry (DGV). The signal is then an intensity value which corresponds to a frequency shift or the velocity data, respectively.

LDV - Doppler Difference Method

Fig. 3.3 shows a schematic of a LDV dual-beam configuration, also known as Doppler difference method. For this the output from a laser is split into two beams. Both beams are focused onto the same point to form one measurement volume. Light scattered from this region can be collected by another focusing lens. Thus, reflections from both beams are then mixed on a detector surface. Analogous to Eq. 3.2 the Doppler shift appears twice, but for both of the beams. Following Eq. 1.14 (Chapt. 1.1.3) and Eq. 1.23/ 1.26 (Chapt. 1.2.1) the photoreceiver signal can be expressed as

$$i_p = i_{DC} + i_{AC} \cos(\omega t) \tag{3.3}$$

wherein the AC part includes the frequency difference between the Doppler shifts of the two beams. Thus, the system is sensitive to velocities orthogonal to the bisector of the two incident beams

$$v_p = \frac{\lambda_0}{2 sin\Theta/2} \cdot \frac{f_{shift}}{cos\alpha} \tag{3.4}$$

This equation is valid for either backward scattering or forward scattering setups.

LDV - Reference Beam Method

The reference beam LDV configuration was the first reported by Yeh & Cummins (1964). In the reference beam technique light scattered from one illuminating beam is collected and mixed with a reference beam on a photodetector. A simple schematic

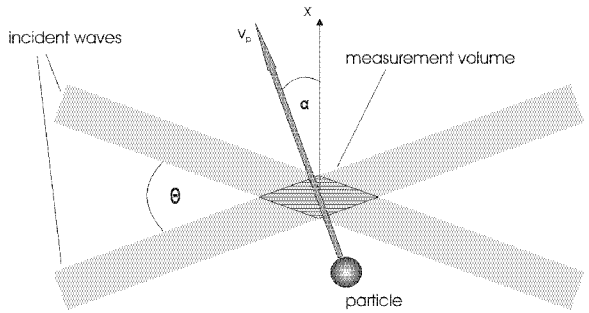

Fig. 3.3: LDA dual-beam configuration.

of this configuration is shown in Fig. 3.4. In a Michelson interferometer configuration the output from a laser diode is split by a beam splitter to form the signal and reference beam. One output is focused to form the measurement volume. Light scattered from this region is collected by the same lens. The reference beam is reflected by a plane mirror. Both backreflected beams are recombined at the beamsplitter and heterodyned on a photodiode.

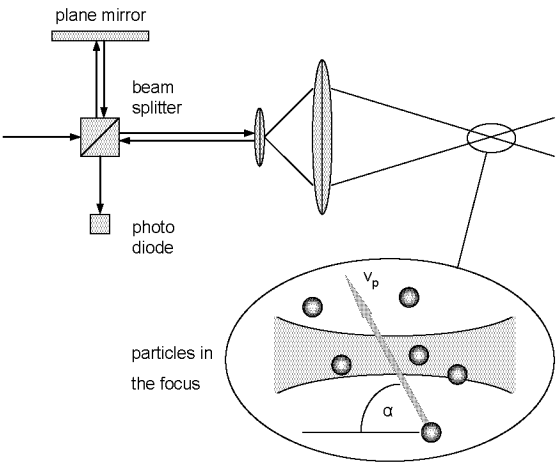

Fig. 3.4: Basic principle LDV - reference beam method.

The Doppler shift depends on the incident angle to the flow direction and on the velocity of the flow. The flow velocity in backward scattering setup can hence be expressed as

$$v_p = \frac{\lambda_0}{2sin\alpha} \cdot f_{shift} \tag{3.5}$$

with α as the incident angle to the flow. In a forward scattering configuration, the Doppler shift is of opposite sign.

3.3 Laser-2-Focus Systems (L2F)

3.3.1 Principle

The L2F principle is based on the measurement of the time of flight of a particle crossing a light gate formed in the flow by two highly focused laser beams (see Fig. 3.5). The distance F_d between the two focal points depends on the optical setup, common values are 100 μm to 400 μm. The length F_l of the focal points is almost of the same order. The focal diameter $F_\emptyset$ lies between 5μm and 15μm, which allows the detection of very small particles (smaller than 1 μm).

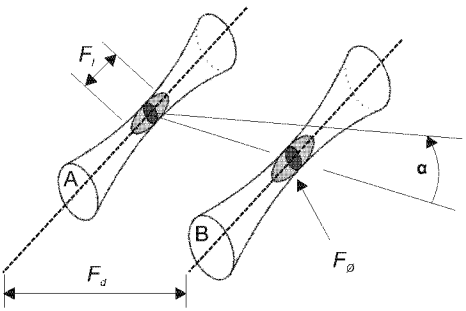

Fig. 3.5: L2F orientation of the measurement volumes.

The reflections from particles passing the focal points can be detected in either backward or forward scattering configuration. In the latter case the scattering levels are much higher, see Chapt. 3.1. The time of flight t_f between two reflection pulses from a single particle passing laser beam A and laser beam B corresponds directly to the velocity vector (direction A to B)

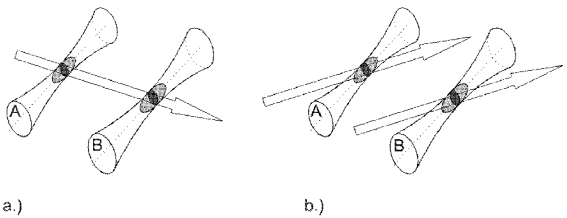

Fig. 3.6: L2F flow orientation a.) correlation possible b.) no correlation.

$$\mathbf{u}_{AB} = \frac{F_d}{t_f} \tag{3.6}$$

Reflection pulses in a L2F setup can be classified into correlated and uncorrelated events. Correlated double-pulses are from a single particle passing beam A and B. The corresponding velocities vary around a certain mean value with a distorted Gaussian distribution, whose variance correlates with the degree of turbulence. Since correlated events are only possible if a particle may pass both beams, the orientation of the light gate has to match with the flow direction, see Fig. 3.6. Otherwise only uncorrelated events from reflections of different particles will be detected, uniformly distributed over the measurement time.

To characterize a full flow, generally a series of measurements has to be done at different orientations within the angular range where correlated events are expected. The statistical analysis will result in a three-dimensional Gaussian distribution curve in terms of angle and velocity, see Fig. 3.7. The maximum of this distribution curve then defines the velocity vector $\mathbf{u}$ in the absolute coordinate system.

In order to distinguish between correlated and uncorrelated events two analysis methods are common, the correlation method and the histogram method.

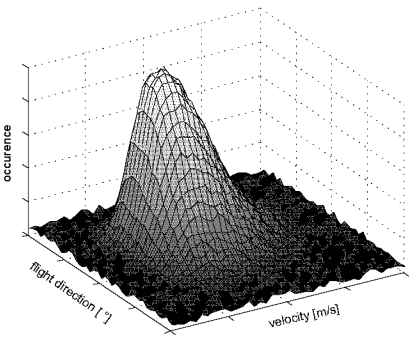

Fig. 3.7: 3D distribution curve of a L2F measurements series.

3.3.2 Correlation Method

The correlation method determines the analogy function of signals, the correlation function respectively. One distinguishes between auto-correlation and cross-correlation. The auto-correlation function gives a value for the self-similarity of a signal (only one detector is used for the beams A and B). The cross-correlation instead gives a value for the similarity between two signals. The auto-correlation is built by the integral of the product of a signal $s(t)$ and the same but shifted signal $s(t+\tau)$

$$\mathscr{A}(\tau) = \int_{-\infty}^{\infty} s(t)s(t+\tau)dt \tag{3.7}$$

For the cross-correlation $s(t+\tau)$ must be replaced by a second signal $g(t+\tau)$. In case of a time dependent measurement, the maximum of the correlation functions can be attributed to the temporal shift within s or between s and g.

In technical use the integral can be discretized with I elements at time steps of τ_s

$$\mathscr{A}(\tau_s) = \sum_{i=0}^{I-1} s(i)s(i+\tau_s) \quad for \quad \tau_s = 0 \ldots I-1 \tag{3.8}$$

This equation gives good correlation results if either the number of elements or the event rate are high enough. An increase of the time steps also gives better correlation values, but causes a trade off in the temporal resolution. Thus, in the majority of cases the correlation method is only used at high event rates (high particle seeding).

The time of flight, as a measure of the flow velocity, can be determined by the position of peaks in the correlation function.

3.3.3 Histogram Method

The histogram method produces a frequency distribution of k time delays between single particle pulses, which directly corresponds to the velocity. One divides the time axis in a certain number of intervals $\Delta_1, ..., \Delta_n$, so-called classes. Every velocity can then attributed to a class $\Delta_j (1 \leq j \leq n)$. The respective quantity Q_j of velocities in a class is the so-called class occurrence. Dividing Q_j by the number k of velocity spot samples gives the relative class occurrence. The uncorrelated velocities, statistically uniformly distributed, build the noise level of the velocity histogram. The correlated velocities are related to a Gaussian curve (see Fig. 3.8). It directly represents the statistical behavior of the flow situation.

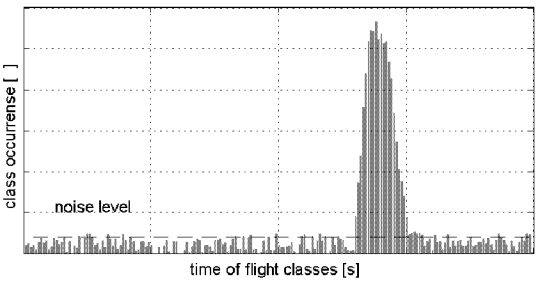

Fig. 3.8: Statistical distribution of a L2F measurement at a fix angle.

The drawback of this method lies in the determination of the time delays between the pulses. In a highly seeded flow the probability increases that several particles are in the light gate at the same time. This creates an unproportional increase of faster velocities. In addition it also makes a simple determination of the pulse delays impossible. Thus this method is often used at low event rates, like in synthetically seeded flows.

Part II

Tip Clearance Probe

Introduction and Motivation

A turbine rotor must have a small but finite clearance to its surrounding casing. This tip clearance is typically about one percent of the blade span. The leakage flows, i.e., fluid flowing through the gap between the blade tips and the shroud of a turbine or compressor, have large effects on the aerodynamics of the machinery and are responsible for a significant percentage of overall losses in turbines (Sieverding, 1985). Due to different thermal expansion coefficients and heating rates in the turbine rotor and the machine casing, the tip clearance is not constant, but depends on the operating condition and varies during machine start-up and shut-down. In order to increase the turbine efficiency, the tip clearance has to be as small as possible, while avoiding damage by blades touching the casing. Therefore, it is important to measure and monitor the tip clearance under operating conditions.

Current tip clearance probes are mostly of inductive or capacitive type, with typical relative accuracies of about 5 % (Sheard et al., 1999; Steiner, 2000). This is sufficient in situations where the probe can be mounted flush with the turbine casing, because the absolute errors are then small. In harsh and high-temperature environments, such as in the early stages of gas turbines, this mounting scheme is not feasible. The Curie point of rare earth metals, which is well below operating temperatures in turbines, sets an upper bound on the maximum operation temperature of these classical sensors (Barranger & Ford, 1981; Dhadwal & Kurkov, 1999). Probes can be mounted in a cooled recess within the casing, but techniques are required with sufficient absolute accuracy over the increased total distance (tip clearance + recess). Optical measurement probes can provide the required resolution and are generally not affected by temperature effects, e.g., (Barranger & Ford, 1981; Pfister et al., 2005). Although the implementation of sensitive optical parts within the turbine is challenging, operating temperatures up to 900 K have been reported (Rooth & Hiemstra, 2001). Also microwave type clearance sensors (Geisheimer et al., 2004) were reported to operate at high temperatures.

A new approach based on optical low coherence interferometry is reported here. The novel tip clearance probe yields near real-time, blade-to-blade tip clearance data with absolute measurement errors in the order of tens of microns even in harsh environments with limited optical access. The measurement technique relies on the interference between backreflected light from the blade tips during the blade passage time and a frequency shifted reference. Due to the measurement principle the absolute spatial accuracy only depends on the coherence length of the light source, rendering the system insensitive to the measurement distance, turbine vibrations and large temperature changes. For typical scenarios where the tip clearances are within a range of a few millimeters, the technique can yield data once every second for each blade. This allows to monitor transient effects during turbine start-up and shut-down. Optical access is provided by a single optical fiber of arbitrary length. The robust sensor head can easily be mounted in a cooled recess. Its own

maximum operating temperature is about 1000 K. The high operating temperature of the sensor itself together with additional cooling possibilities allow the use of the system in environments with temperatures which are much higher, but standard in today's gas turbines. The sensitive mechanical, electronic and optical components of the system are placed far from the turbine in a separate post-processing unit.

The presented prototype of such a system is an all-fiber assembly, with self-calibrating capabilities and a spatial resolution of less than 50 μm. The data acquisition system consists of a digital storage oscilloscope and a common PC. The limited data transfer rates of this system lead to reduced scan rates (typically one per minute). Results from proof-of-principle measurements at different turbines, the LISA test facility at ETH Zurich and the GT26 gas turbine at ALSTOM, are reported in this thesis.

4 Turbomachinery Background

4.1 Tip Clearance/Leakage Flows

The clearance between the tip of the rotating components (compressor or turbine blades) and the shroud is inevitable in turbine engines. The leakage flow across this gap is caused by the pressure difference between the pressure side and suction side of the blade. This flow can have significant effects on the stage aerodynamic performance and on the structural durability of the blade. In the case of hot gas turbines the special flow situation across the blade tip can result in hot spots in this blade region. Therefore, different cooling schemes, e.g., film cooling, are applied to improve the durability of the components.

The leakage flow tends to roll up to form vortices beginning at the blade tips, see Fig. 4.1. The interaction of this secondary flow with the main flow causes complex flow phenomena with many of detrimental effects on the performance of an axial turbine. The induced complex three dimensional flow field can span up to 20% of the blade beginning at the tip.

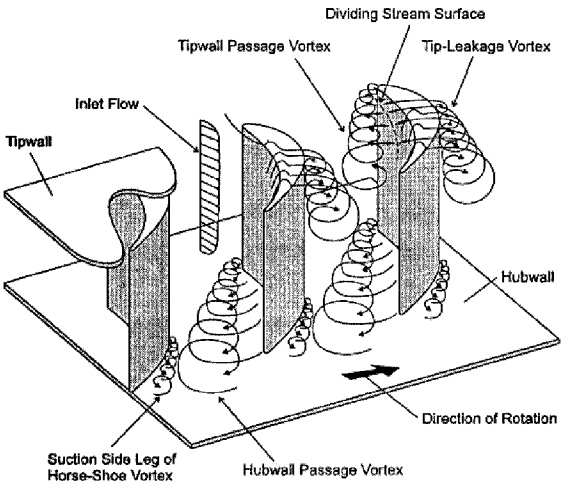

Fig. 4.1: Secondary flow field of an axial-turbine stage (Sjolander, 1997).

4.2 Clearance Effects in Turbines

As mentioned the secondary flows caused by the gap between blade tip and turbine casing can have large impacts on the turbine operation and its efficiency. A whole research field is occupied with the analysis and simulation of this complex issue. Two of the main and obvious effects are loss generation and the change of heat transfer.

4.2.1 Losses

Tip clearance losses are responsible for a large fraction of the overall loss in a turbine. The average loss level is about 25% of the total loss and 33% of rotor loss. As an example, Fig. 4.2 shows the percentage of losses for different effects in comparison to the total loss of several turbines (13-CYL, 13-CONE, 12, etc.). It can be seen that even small changes in the tip clearance have direct effects on the turbine efficiency.

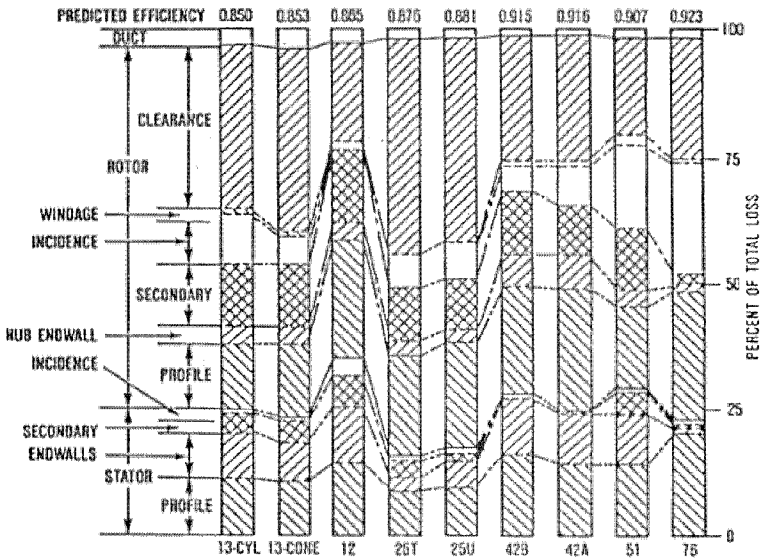

Fig. 4.2: Sources of turbine losses (Booth, 1985b).

A conceptual model (see Fig. 4.3) shows that not only the reduced area of the blade lowers the efficiency, but that leakage mixing and unloading effects cause additional losses. For example, the efficiency decrement of 4% is 1.5 times higher than the normalized change of tip clearance (2.6%).

Efficiency measurements also show that the tip clearance loss is much higher than the reduced area ratio, see Fig. 4.4. The broken curve shows a good consistence

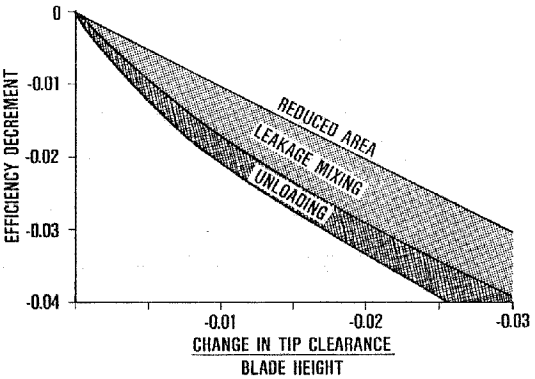

Fig. 4.3: Loss vs. reduced blade area (Booth, 1985a).

between prediction and experiment of the dependence of the normalized tip clearance and loss of efficiency in percent. Again the loss of, e.g., 5% is much higher than the tip clearance increase of 2%. As a rule of thumb (Schaub et al., 1993), in a high performance high pressure turbine stage 45% of the losses in the roter and 30% of the losses in the stage are attributable to the tip leakage flow.

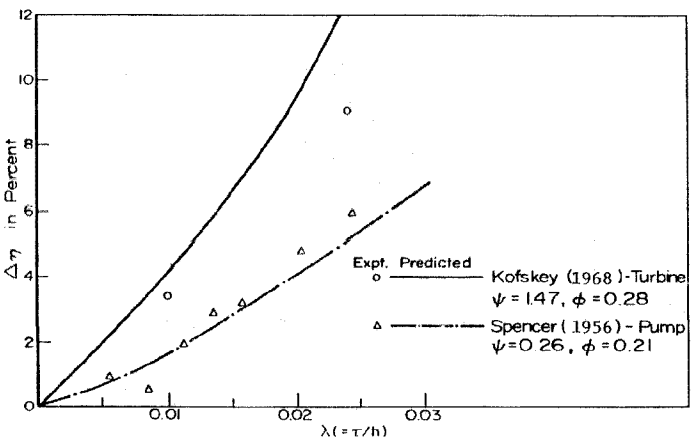

Fig. 4.4: Turbine efficiency vs. tip clearance (Lakshminaryayana, 1985).

4.2.2 Heat Transfer

Heat transfer from a fluid to the surface of a body depends not only on the material and fluid, but also on the flow situation around the surface. The heat transfer coefficient can vary over a wide range depending on the flow field. The flow field dependent heat transfer coefficient thus yields heat fluxes in the tip region, which are different from those found over other parts of the blade. Hot spots are possible, which lower the structural durability radically or may destroy a turbine blade directly. Turbines operate at very high temperatures, the first stage behind the combustion chamber in particular. Hence, the cooling of this stage is of special importance.

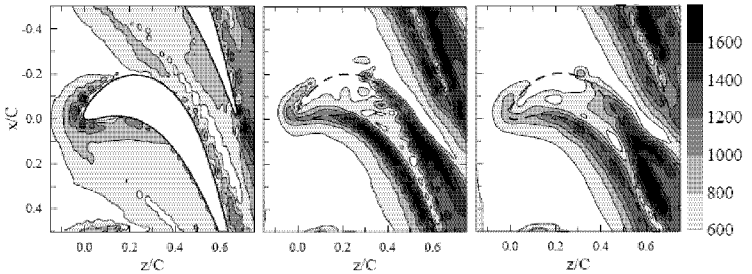

Fig. 4.5: Sheerwood number representing amount of heat transfer (Cho et al., 2000).

For example, Fig. 4.5 shows contour plots of the Sherwood number, representing the amount of heat/mass transfer, on a blade tip for various tip gaps. The Sherwood number without gap is shown on the left, in the middle panel the gap is 1.5 mm and 3.0 mm on the right. Without a gap the heat/mass transfer enhancement due to horse-shoe vortices is observed at the leading edge of the blade. Additional local peaks caused by the wake at the trailing edge are also existent. Increasing the clearance between the blade tip and shroud, fluid enters the gap on the pressure side. As a result, the Sherwood number characteristics on the blade tip changes significantly. For example, a hot spot is generated on the blade tip trailing edge at 3 mm tip gap.

5 Experimental Setup

5.1 Measurement Principle/Optical Arrangement

Fig. 5.1 shows the schematic setup of the optical components in the measuring circuit of the system. A superluminescent diode (SLD, Superlum Diodes model SLD56-HP2, 10 mW) emits low coherence light into a singlemode fiber. A fiber optical isolator protects the sensitive light source from backreflections and guides the light to a polarization insensitive optical circulator. The circulator is used to transfer the light through a singlemode optical fiber to the endoscopic front end (EFE), where a collimator lens directs the light out of the fiber onto the passing blade tips. From there a small fraction of the incident light is reflected back onto the collimator lens and into the fiber towards the circulator, where it is deflected into the interferometer part of the measurement system. A small fraction ($\sim$ 1 %) of the light is also reflected off the two surfaces of the collimator lens, which provides a spatial reference.

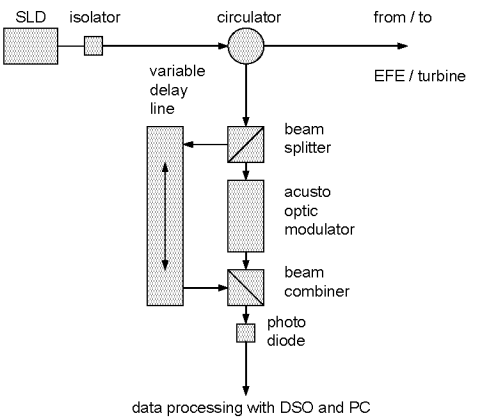

Fig. 5.1: Schematic setup of the optical parts for the tip clearance probe.

Following the nomenclature of Fig. 5.2, the light reflected from the blade tips is denoted as ray 1, the light reflected from the lens front and back surfaces as rays 2 and 3 and the light from the fiber end as rays F, respectively. The light backreflected from the turbine blades and the front end (rays F, 1, 2, 3) is fed into two interferometer arms by a beam splitter. In the reference arm, an acousto-optic modulator (AOM, NEOS model 26055) shifts the frequency of the light by 55 MHz, corresponding to several periods within the blade passage time ($\sim$ 10 μs). The delay arm contains a motorized variable delay line (VDL, General Photonics VariDelay). The light from the two interferometer arms is recombined by another beam splitter/combiner and a broadband photoreceiver (New Focus model 1811) serves as detector.

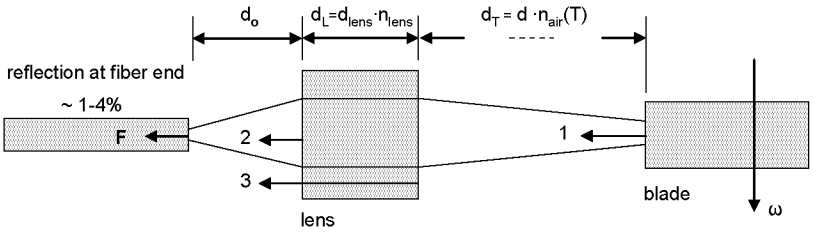

Fig. 5.2: Interaction between laser beam, front end and blade tip.

As shown in Fig. 5.2, the path length of ray 1 is longer than that of rays 2 and 3 or even ray F. Denote the tip clearance as d_T, the optical thickness of the collimator lens as d_L, the distance between fiber end and lens as d_0 and the path lengths of both interferometer arms (between the two beam splitters/combiners) as l_r and l_d, respectively. If the VDL is set such that $l_r + 2(d_T + d_L + d_0) = l_d$, for example, the part of ray 1 going through the reference arm interferes with those parts of ray F which go through the delay arm. The frequency of the AOM is now recorded as a beat signal at the detector, which can be detected as a peak in the power spectrum. Similarly, interference between ray 3 and ray F is observed, when $l_r + 2(d_L + d_0) = l_d$. This represents the lens back surface, whose position within the turbine is known. In addition, by checking the delay setting where ray 2 and ray F interfere, i.e., when $l_r + 2d_0 = l_d$, the EFE can be monitored for failures.

5.2 Optical Frontend

As mentioned the sensitive optical parts and electronics are included in a separate self-contained unit, placed sufficiently far away from the turbine. Only a singlemode fiber is needed to connect the interferometer part with the sensor front end, positioned within the turbine casing. The length of this connecting fiber is arbitrary. For the test described in this thesis it was measuring approximately 20 meter.

The two meter long fiber optical sensor front end (Fig. 5.3) was custom-made by the company "Fiber-Optic" in Spreitenbach, Switzerland. Its maximum operating temperature is about 1000 K. Besides a standard fiber connector it consists of a gold coated singlemode fiber. The fiber is placed within a flexible steel wire sleeve. Within this sleeve the fiber is free to move, such to avoid stresses due to different thermal expansions. At the front end's upper side is an approx. 1 cm thick and 30 cm long bent tube with a built-in fiber connector (a part of this tube is also flexible). The tube consists also of a Swagelok connector for the installation within the turbine casing. At the lower side of the front end a focusing sapphire lens, approx. 1.5 mm in diameter, is embedded. The lens and a part of the fiber end are bonded and permanently crimped together with the surrounding metal jacket. The placements of fiber and lens are as described in Fig. 5.2.

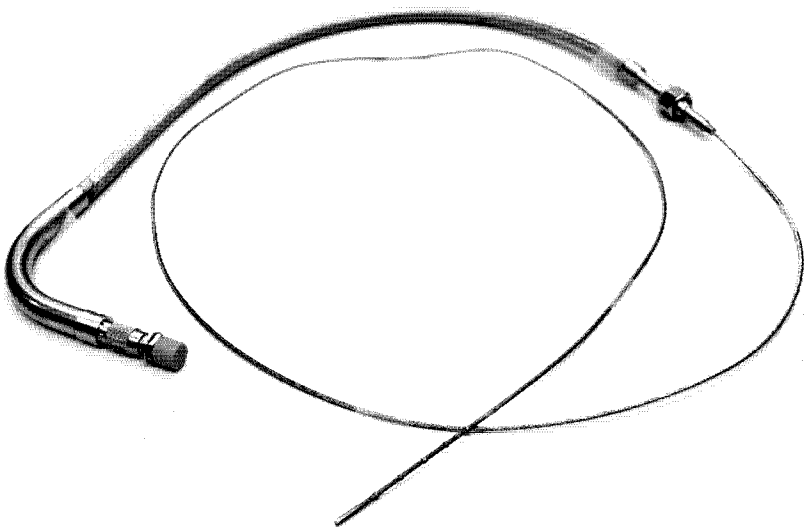

Fig. 5.3: Photograph of the tip clearance probe SFE.

For the test at ALSTOM's GT26, the front end was inserted into a tube within the turbine casing. At one end the sensor head was pressed against a stop position close to the turbine blades. Thereby approx. the last 20 cm of the sensor's steel sleeve are guided inflexibly to avoid movements of the sensor head during the turbine operation. The rest of the tubing within the casing was flexible, i.e., able to follow any movements of the turbine casing introduced through different thermal expansions or force loads. Through the Swagelok connector the tubing was sealed to the outer environment of the turbine, such that it could be pressurized with cooling air. Besides the cooling purpose this air stream also prevented the contamination of the lens surface exposed to the inner flow streams of the turbine by a constant wash-up.

5.3 Signal Processing

5.3.1 Data Acquisition

Fig. 5.4 shows the data acquisition chain used for the tip clearance experiments. The analog signals from the photoreceiver are first filtered by a bandpass filter (Mini Circuits BIF-60) and then amplified by 36 dB with a high speed amplifier (Hamamatsu C5594-12). The preconditioned signals are then digitized with 8 Bit precision by a

Digital Storage Oscilloscope - DSO (LeCroy LT347L). Data is then transferred to a PC through a 10 MBit Ethernet connection for further analysis and storage. The sampling rate and the acquisition window length are set through the DSO. The DAQ is initiated by triggering the DSO with an external key-phaser of the test facility.

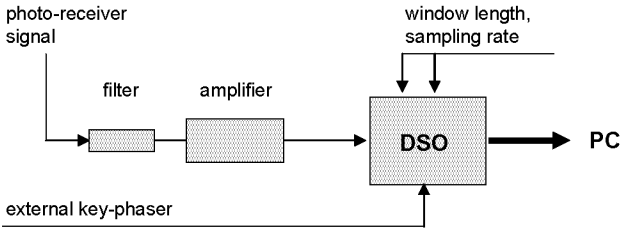

Fig. 5.4: Data acquisition - tip clearance probe.

5.3.2 Data Analysis

Two LabView (Ver. 7.1, National Instruments) programs perform the data storage and analysis. While one of them only stores the raw data for later analysis, the second extracts tip clearances either on-line or from previously stored data sets. During the critical gas turbine tests, data was initially stored. The raw data is first bandpass filtered with a second-order Butterworth IIR-filter at a frequency range of 55 ± 1 MHz. A reliable indicator of a blade passage at the current delay line setting was found to be the product of the signal variance and the maximum of the power spectrum within a few microseconds sliding window. Either one of these factors on its own did not yield a satisfactory discrimination between blade passages and noise, especially at low signal levels. This product will be referred as beat signal intensity for the remainder of this part of the thesis. Suppose that data is acquired for the entire duration of a turbine revolution. The VDL delay is varied in steps after each acquisition and a new full-revolution trace is acquired. The step size for the VDL has to be less than the coherence length of the light source. This, combined with the given rotation rate of the turbine and the desired measurement range, is an upper bound for the detection rate of the technique. A full scan over 1 mm in steps of 40 μm on a turbine operating at 50 Hz thus requires at least 1 second. Note that data acquisition and moving the VDL occurs during alternating revolutions. In practice, achievable data transfer rates and the response time of the VDL motor led to increased scan times.

Two approaches to reduce the amount of raw data were used. One is undersampling of the DSO at sampling rates of 50, 20 and 10 MHz. The Butterworth filter then had a frequency range of 5 ± 1 MHz. Noise from multiple frequency ranges is convolved into the relevant frequency range.This leads to reduced signal-to-noise ratios (SNR). For tests in turbines, however, it was found to be practical. A further reduction of the amount of data can be realized by only acquiring data within short windows around the expected blade passage time. For turbine stages with many blades and using window sizes which capture the blade passage reliably, however,

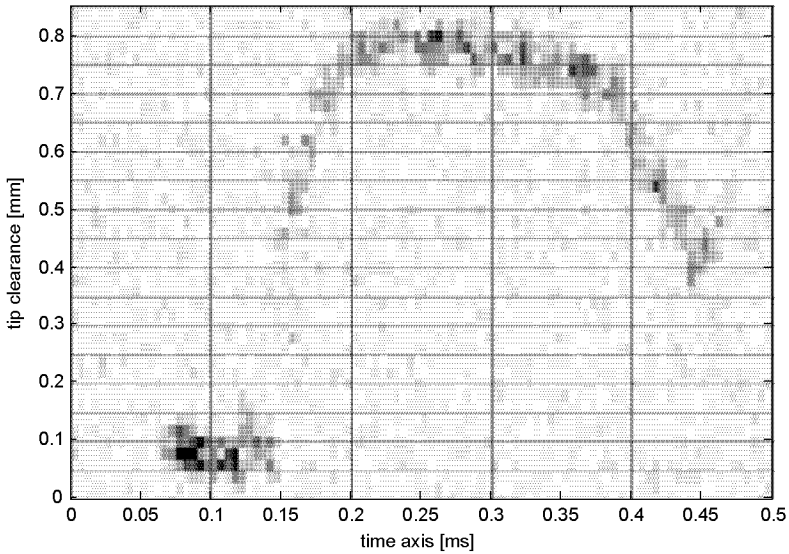

Fig. 5.5: Sample intensity map for a turbine blade on a rotary stage, 40 μm delay steps, 5 μs sliding window.

the benefits are small. If the SNR is low averaging over several revolutions can be employed. Averaging is then performed over the beat signal intensities.

The signal analysis produces a two-dimensional map of the beat signal intensity, i.e., intensity vs. the delay line setting and time within each revolution. An example map is shown in Fig. 5.5. It represents the passage of a used gas turbine blade mounted on a simple test rotary stage at ETH Zurich. The test was performed under room temperature condition, the rotational speed was around 6 Hz, which resulted in a tip speed between 25 and 30 m/s. The intensity value is color-coded, a large value of the beat signal intensity (dark color) indicates that a blade passage at the set path length difference has been detected. The vertical length of the lines depends on the coherence length of the light source and the step size of the VDL, representing the system's spatial resolution. In Fig. 5.5 the step size was set to 40 μm. The temporal resolution, i.e., the width of the lines depends on the size of the sliding window for the analysis, here 5 μs. The smaller this window is chosen, the lower is the SNR of the beat signal intensity. This sets the lower bound for the temporal resolution. Averaging of intensity maps with a phase-lock to the rotation speed increased the SNR. Please note, due to phase jitter of the beat signal, the averaging of the raw photoreceiver signal over a number of blade passages is not possible.

6 Experiments

6.1 System Performance

6.2 LISA Turbine Tests

LISA, Fig. 6.1, is a research turbine test facility of the Laboratory of Turbomachinery at ETH Zurich. The important design features are mechanical precision, full accessibility for instrumentation as well as quick assembly. The core of the test rig is an axial turbine with vertical orientation. The maximum power of 400 kW is taken from a quasi atmospheric air circuit driven by a 750 kW radial compressor. The turbine's power output is connected via an angular gear box to a generator with electrical power feedback. The air circuit consists of a cooler, which controls the inlet temperature, a flow conditioning segment and a calibrated venturi-nozzle integrated into the back flow pipe (Pfau, 2003). The results of LISA tip clearance tests presented in this thesis were performed as a secondary application during tip gap flow field manipulations (Behr et al., 2006).

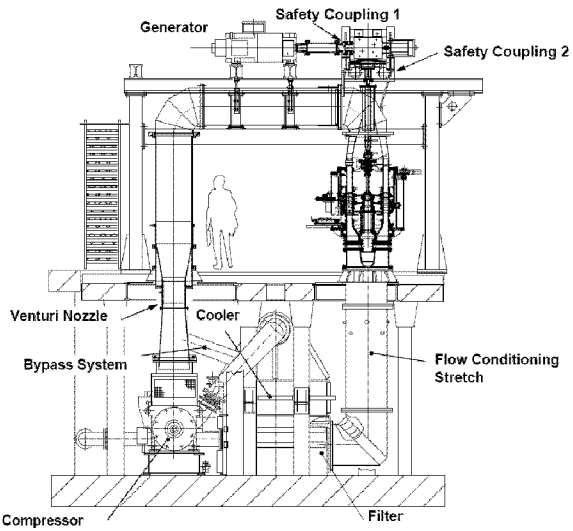

Fig. 6.1: Schematic view of LISA axial test turbine (Pfau, 2003).

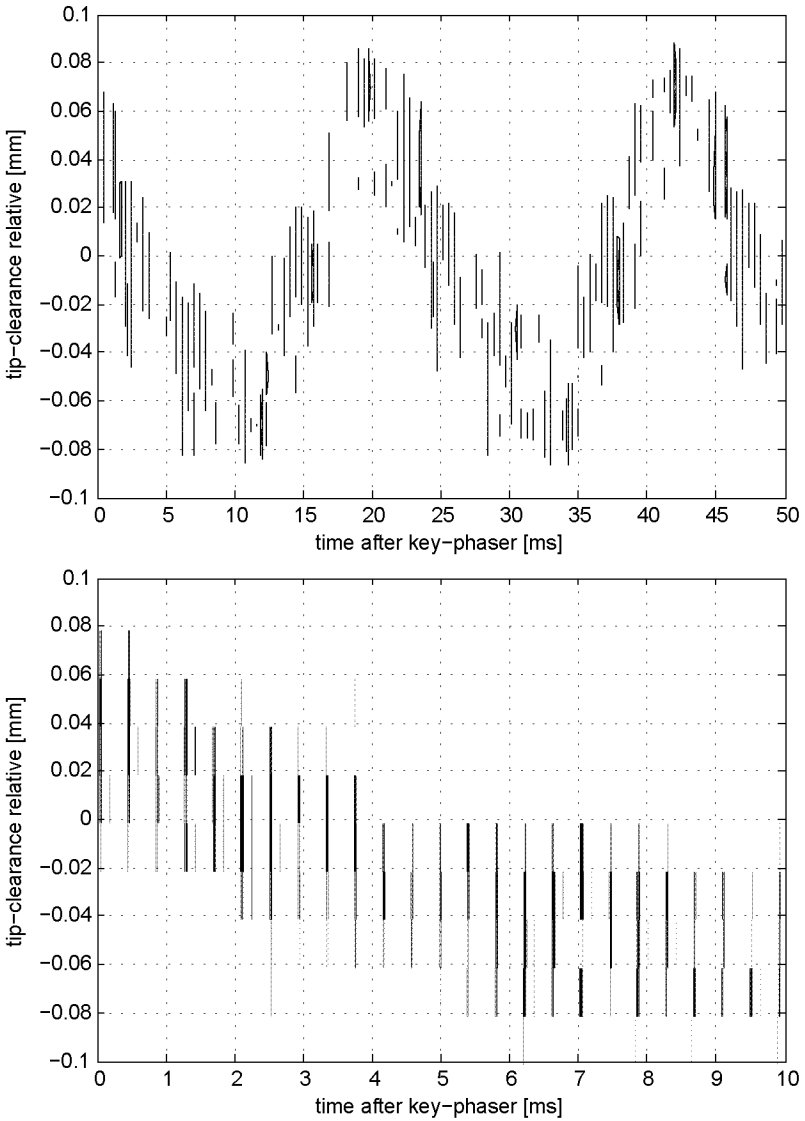

Fig. 6.2: Tip clearance distribution of LISA rotor, intensity map [11].

[11] The full view suggests that not all blades were detected. The detail view in the lower panel, however, shows that this is just an artifact of the visualization routine.

Due to the high mechanical precision of the turbine as well as the use of cold gas (approx. 50°C) and therefore small thermal expansion responses, the primary objective of the measurements was to scan with high spatial resolution, i.e., small interferometer delay steps. Fig. 6.2 shows a two-dimensional beat signal intensity map of 50 milliseconds at a rotation speed of 2700 rpm, i.e., spanning two full revolutions. The sampling rate was set to 50 MHz, the step size to 20 μm. The complete scan over 0.3 mm lasted 60 seconds. The rotor with a tip diameter of 798.6 mm [$\pm$ 0.01 mm] consists of 54 blades machined into one single aluminum ring by electrical erosion. The smooth aluminum surface of the blade tips yields a high backreflection level. Together with the signal amplification due to the interference with the reference reflection in the EFE, the SNR in these tests is not critical. The rotor blade tips show a sinusoidal clearance behavior with an amplitude of approx. 50 μm. This value might be due to a small eccentricity of the rotor assembly within the turbine.

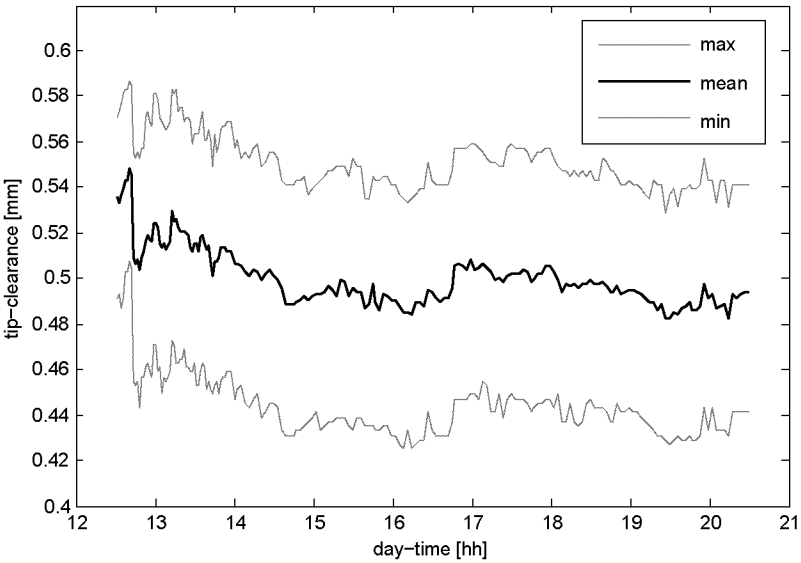

Fig. 6.3: LISA tip clearance behavior over operation time.

In Fig. 6.3 the average, the maximum and the minimum tip clearance of the 54 blades was recorded over time. The sampling rate was set 10 MHz and the step size to 20 μm. In this test, a separate spatial reference was provided by a window which was placed approximately flush with the casing. The scan range was increased to 1.15 mm such to include this reference location as well. A scan then lasted 95 seconds. The long-term clearance behavior of the turbine shows a small decrease of the gap by about 100 μm (before 13 hours daytime, the turbine was rotating at a lower speed). In addition a smooth increase and decrease of the tip clearance can be detected. This might be due to a slow gradual rotation of 20° of the turbine casing during the simultaneously performed flow field measurements.

6.3 GT26 Gas Turbine Tests

The GT26 gas turbine is developed for combined cycle applications. It is designed to burn natural gas as a primary fuel and diesel as backup fuel. In terms of operational flexibility, the GT26 can be found operating in all three major modes: base load, intermediate duty and daily start/stop. At 50 Hz rotation speed and in combined cycle the GT26 delivers approx. 281 MW electrical output (about 260 MW are directly related to the gas turbine). Its smaller counterpart is the GT24 with approx. 188 MW electrical power. The GT24/GT26 are provided with a sequential combustion system consisting of an environmental (EV) and a sequential combustor (SEV), see Fig. 6.5. The sequential combustion system is unique to the ALSTOM GT24/GT26 gas turbine type and applies the thermodynamic reheat principle (ALSTOM Power, 2006).

The tests at GT26 were primarily performed to demonstrate the performance of the measurement system under operational conditions, i.e., high temperatures and weak reflection levels from the coated turbine blades, as well as the short passage time of the blades (approx. 10 μs). Tests were performed at the first stage behind each combustor in the major operation modes, with gas or oil as fuel. Due to confidentiality aspects, the results of these tests cannot be illustrated in detail within this thesis. Fig. 6.4, as an example, shows only a part of an intensity plot (please note: the absolute tip clearance values have been changed). The delay step value was set to 40 microns, which in turn is the measurement accuracy. Larger step values are

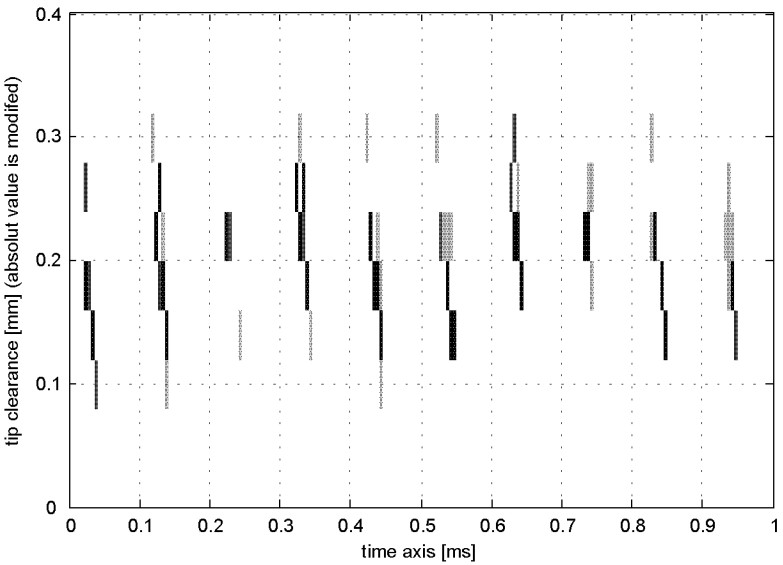

Fig. 6.4: GT26 example intensity plot of several blade passages.

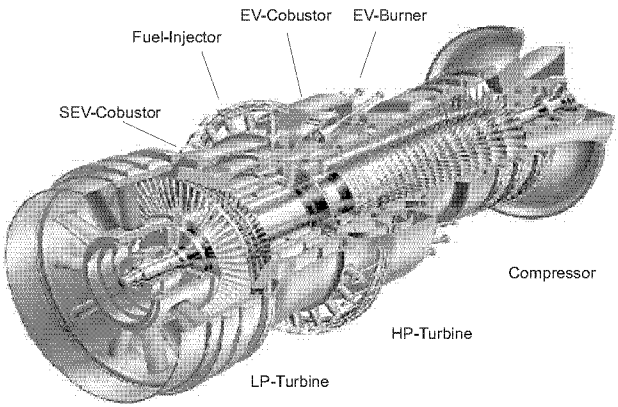

Fig. 6.5: GT26 schematic illustration.

not possible, due to the coherence length of the light source of approx. 50 μm. The time axis is resolved with 5 microseconds. The signatures show that the blade tip is not flat, but slightly beveled.

In general it can be said that even under real gas turbine conditions, the sensor still works well. However in terms of measurement system performance a few issues need to be addressed. The EFE with its optical parts close to the hot gas flow showed no irreversible failures. The high temperatures and the mechanical loads due to the casing movements during its warm-up did not damage the optics. The 20 m fiber optical extension cable also withstood the temperatures within the turbine enclosure, which can reach up to approx. 80°C close to the turbine. The SNR was high enough to operate with a sampling rate of 50 MHz and without averaging. During the start-up of the turbine, i.e., the first 30 minutes after ignition, the SNR was comparatively low and just above the sensing limit. Furthermore, after 5 hours of operation under base-load conditions, the SNR dropped over a period of 20-30 minutes. Finally and reproducibly in two tests at around 5-6 hours of operation, the SNR was too low to detect any tip clearances.

Both phenomena are probably caused by changes in the thermal behavior of the optical fiber within the casing and the turbine enclosure. The first decrease of the SNR at the start-up might be due to the fast temperature rise and therefore the huge thermal stresses at the EFE. After 30 minutes, the rate of the temperature rise is decreased. The whole EFE is heated-up and due to its design the fiber within the EFE experiences no mechanical stresses. The second decrease can be attributed to the relatively small thermal load in the turbine enclosure. The extension cable was protected by a thick PVC tube (standard telecom cable). Its thermal insulation might cause the long response time to the temperatures in the enclosure building. The assembly of the fiber and the PVC is not specifically designed to balance mechanical stresses of the fiber at higher temperatures. Thus, under stress the fiber

transmissivity can drop by orders of magnitude. However, both assumptions have to be investigated in further tests.

During the GT26 tests the beat signal frequency was shifted by 10 to 15 MHz. This is due to Doppler shift in the backreflected light from the blade tips. If the surface of the blade tips moves not perpendicular to the sensor head, a Doppler shift can be detected as in reference beam LDA applications, see Chapt. 3.2.2. Any relative velocities parallel to the beam axis between the reference reflection and the blade reflection will result in a Doppler signal. In the GT26 the blade tips are relatively rough, plus they are slightly beveled. The roughness leads to a spectral broadening of the beat signal frequency of up to $\pm$ 2 MHz. The bevel of the tip causes a general frequency shift. It might also be possible that the sensor was mounted at a small angle. Taking into account the circumferential velocities at the GT26 of approx. 350 m/s, the observed frequency shift corresponds to an angle of about 1 - 2^o off the normal direction.

In the data acquisition and analysis this Doppler shift has to be considered. All bandpass filter devices have to match the shifted frequency. For industrial applications such uncertainties in the analysis regime should be avoided.

7 Conclusions / Outlook

Proof-of-principle measurements were presented for a novel tip clearance measurement technique with high spatial and temporal resolution. Independent of the distance between the output coupler lens and the blade tip the absolute spatial accuracy is within 50 microns. Variations in fluid or material temperatures have no influence other than minimal changes in the refractive index. Data acquisition rates for tip clearance profiles on the order of seconds allows monitoring of transient effects during turbine start-up and shut-down. Simultaneously with the tip clearance, the blade passage times are measured, facilitating the detection of blade oscillations.

The tests at the LISA turbine test facility and the GT26 gas turbine under operating conditions already led to qualified results. For the first time the tip clearance behavior from the first stage of a large scale gas turbine cold be monitored for different engine loads. However, for a second prototype the aspects of industrial operation have to be considered. One focus is the thermal behavior of the optical fibers close to the turbine. In particular the problem in long-term tests has to be solved. The exposure of the optical connection cable to an environment of 80^oC leads to a reversible failure after approx. 5 hours. With special assemblies the optical fiber in the covering tube can be guided stress-free, which should solve this problem.

The second focus for further developments lies in the observed Doppler shifts, which lead to a shift of the beat signal. On one hand, with this the acousto-optic modulator with its fixed frequency shift is unnecessary. On the other hand, depending on the mounting orientation of the sensor to the blade tip surface and blade tip velocity, the Doppler shift will have different values. For this reason, a flexible demodulation of the signal into a fixed frequency band might be one possible technical solution. This is particularly important in a situation where one signal processing unit operates with more than one sensor front end, which is an additional possible improvement for the system. Therefore, tests with amplitude modulated SLD and a following frequency lock-in have been made with promising results.

With the use of an optical multiplexer measurements with a series of sensor front ends mounted around the circumference of the turbine casing are possible. Still only one light source and one signal processing unit are necessary. The multiplexer just needs to be inserted between the circulator and the front ends. Then the tip clearance for each sensor position can be measured successively. The increase in the measurement time for this scenario is minimal, since it should be possible to switch between two sensor front ends within one or two turbine revolutions.

Part III

Self-Referencing Velocimetry

Introduction and Motivation

Velocimetry techniques for boundary layer measurements face two challenges: spatial resolution and non-intrusiveness. In most technical applications, the thickness of the boundary layers is on the order of millimeters such that sub-millimeter resolution is required for meaningful measurements. The requirements are even higher when the viscous sub-layer and the log-layer have to be resolved (Schlichting & Gersten, 2000).

Traditionally, hot-wire anemometry (or constant temperature anemometry, CTA, as well as constant current anemometry) has been the method of choice for such measurements, e.g., (Häggmark et al., 2000; Ligrani & Bradshaw, 1987; Wolff et al., 2000). The typical diameter of the wire is on the order of micrometers. They are typically 1-2 mm long, but the spatial resolution in the wall-parallel direction is not critical. Because the measurement location is identical to the probe location, the probe has to be moved to obtain the velocity profile across the boundary layer. This makes this technique problematic for measurements over moving objects. But even over stationary surfaces, the thermal conductivity of the wall leads to systematic errors of the measured velocity (Durst & Zanoun, 2002; Durst et al., 2001).

Recently, micro-PIV has been applied to high-resolution boundary layer measurements. PIV either requires optical access from at least two directions (one for the illuminating laser sheet, the second for the camera) or a depth resolving focusing optic as in microscopy (Lin & Perlin, 1998; Meinhart et al., 2000). Depending on the geometry and the object's movement, this might not be feasible. Laser-Doppler velocimetry (LDV) lacks the required spatial resolution, which is determined by the diameter of the intersecting laser beams and the crossing angle. LDV measures the velocity component perpendicular to the long axis of the intersection ellipsoid. This means that the spatial resolution is poorest in the direction where it is most critical. With a novel technique using a tilted fringe system, the LDV intersection volume can also be resolved in the order of microns (Büttner & Czarske, 2001, 2003). Distributed laser Doppler velocimetry (DLDV) (Gusmeroli & Martinelli, 1991), a reference beam LDV using low coherence light, defines the measurement location as the focal region. The low coherence interferometry then allows further resolution within the focal region. In this respect, the technique shares many aspects with optical coherence tomography (OCT) (Tomlins & Wank, 2005). DLDV can be seen as a very similar technique to the approach described in this thesis.

In a PIV image, the flow is visible together with the object such that it is possible to deduce the measurement location (relative to the surface) from the data without independent knowledge of the object's trajectory. Nevertheless, as mentioned, the PIV installation itself might be very challenging. CTA, LDV and DLDV on the other hand have all in common, that they are not self-referencing. At any instance, the relative location of the object to the measurement volume has to be known. If

the motion is irregular or if the shape of the object changes over time, this might pose a problem.

The new technique is self-referencing with respect to its vertical measurement location to an arbitrary surface and has a spatial resolution only depending on the coherence length of the light source (e.g., see interferogram Fig. 2.3). It measures in-plane and out-of-plane components of the velocity vector. The sensitivity to out-of-plane velocities (which are normally much lower) is tenfold (value can be adjusted) higher than for in-plane velocities. As for LDV and PIV, particle seeding is required. Conceptually, planar measurements (cf. PIV) are also possible with self-referencing capabilities.

The working principle of this new technique is explained using the example of a two-component boundary layer profiler based on the Doppler effect. The systems is spatially self-referenced relative to a surface, but applications where the sensor head is the reference follow the same principle. For the new approach a notation is introduced with "SR" standing for self-referencing, i.e., SR-LDV.

8 Self-Referencing Low Coherence Velocimeter

8.1 Basic Working Concept

The new technique combines flow velocimetry measurements with self-referencing qualities by the use of low coherence interferometry. The measurement location is selected based on its distance from an object. This object can either be the sensor head itself or an external surface, which might be moving relative to the sensor head. The distance can be adjusted without moving optical parts in the sensor head, simply by varying the path lengths in the interferometer arms. Irrespective of any movement of the surface, measurements are always performed at a set distance from the wall. One could say that the measurement location is in wall-fixed coordinates instead of lab-fixed coordinates as for other techniques. The absolute accuracy of the measurement location and the spatial resolution is on the order of tens of micrometers, depending on the properties of the low coherence light source.

This technical approach is applicable to single-beam single-component measurements, as well as to multi-beam multi-component measurements (cf. Laser-Doppler Velocimetry - LDV or Laser-Two-Focus Velocimetry - L2F). In the future, with a probable rise of power of broadband light sources, two-dimensional measurements (cf. Particle Imaging Velocimetry PIV) might also be possible with self-referencing image planes or a pointwise scanning technique. As mentioned similar to most other optical velocimetry techniques, flow seeding is required.

This chapter outlines the principles of the self-referencing technique for LDV and L2F applications. The new self-referencing aspect will be indicated with the prefix SR, i.e., writing SR-LDV or SR-L2F.

8.2 Self-Referencing Laser-Doppler Velocimetry (SR-LDV)

8.2.1 Measurement Principle - SR-LDV

The system consists of two main parts: the interferometer unit and the sensor head. Fig. 8.1 shows the schematic setup of the optical components in the interferometer unit of the system. A superluminescent diode (SLD, Superlum Diodes model SLD56-HP2, 1310 nm, 10 mW) emits low coherence light into a singlemode fiber. The dotted line in Fig. 2.3 is the autocorrelation function of the SLD. The coherence length is represented as the FMHW of the peak (~ 35 μm). A fiber optical isolator protects

the sensitive light source from backreflections and guides the light to a polarization insensitive optical circulator. The circulator is used to transfer the light through a singlemode optical fiber to the sensor head, where a lens couples the light out of the fiber and onto the object surface.

A fraction of the incident light is reflected back from the surface of the test object onto the lens and back into the fiber towards the circulator, where it is deflected into the interferometer. A small fraction of the light is also reflected off the particles passing the laser beam. Fig. 8.2 introduces the nomenclature used subsequently. Note that the two incident beams are not used simultaneously (this would require a separate interferometer unit for each beam). Instead, it distinguishes between subsequent measurements using different incidence angles relative to the flow. In Fig. 8.2, the reference surface is taken to be the object's surface.

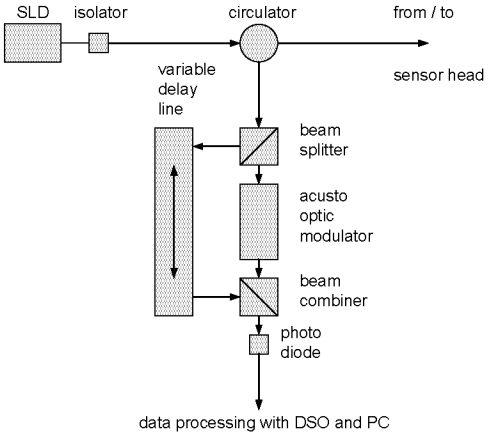

Fig. 8.1: Schematic setup of the optical components in the interferometer unit, which also includes the light source.

Light reflected off the test object surface is denoted as rays 1 and light scattered off the particles in the flow is denoted as rays 2. The letters distinguish between the measurements using different incidence angles and the numbers refer to different reflecting objects.

All light backreflected is fed into the two interferometer arms by a beam splitter. In the reference arm, an acousto-optic modulator (AOM, NEOS model 26055) shifts the frequency of the light upwards by 55 MHz, corresponding to several periods within the short passage time (tens of microseconds) of the particles in the focus. The delay arm contains a motorized variable delay line (VDL, General Photonics VariDelay). The light from the two interferometer arms is recombined by another beam splitter/combiner and a broadband photoreceiver (New Focus model 1811) serves as detector.

Consider a single angle of incidence, e.g., measurement a. The path length of ray $1a$ is longer than that of ray $2a$. Denote the distance between the surface and the particle as d and the path lengths of both interferometer arms (between the two beam splitters/combiners) as l_r and l_d, respectively. If the VDL is set such that $l_r + 2d = l_d$ ("positive delay"), for example, the part of ray $1a$ going through the reference arm interferes with those parts of ray $2a$ which go through the delay arm. In a static situation the frequency of the AOM is now seen as beat signal at the detector. The same phenomena occurs if the VDL is set to $l_r - 2d = -l_d$ ("negative

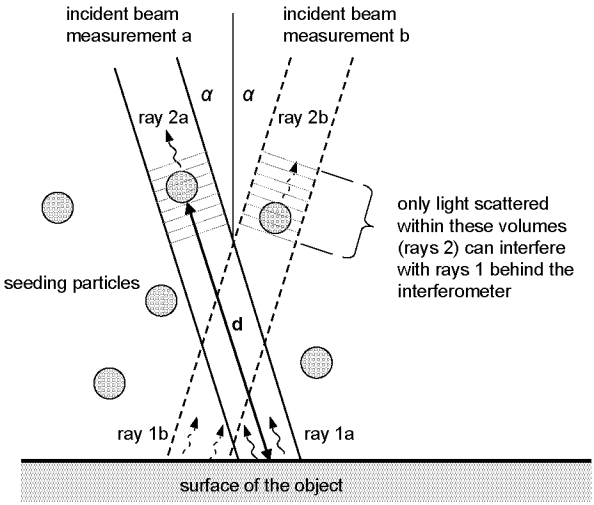

Fig. 8.2: Self-referencing LDV - schematic setup of the interaction between laser beams and particles.

delay"). Then the part of ray $1a$ going through the delay arm interferes with the part of ray $2a$ which goes through the reference arm.

With relative movement between the particle and the surface there is a frequency difference between rays $1a$ and $2a$ due to different Doppler shifts of the two reflections. In case of interference this results in an additional frequency shift of the beat signal relative to the AOM frequency. Normally the surface reflection is orders of magnitude stronger than a particle's reflection, especially for backward scattered light. In case of interference between the two reflections, the large reference signal amplifies the amplitude of the beat note, thus allowing the use of an SLD with relative low optical power. The direction of the shift depends on the setup of the autocorrelator (positive or negative delay) and on the direction of the relative movement between the two reflections. In the absence of interference, no beat signal is present. This means that only those particles produce relevant signals, which are within a thin layer from the surface. The thickness of the layer is approximately equal to half the coherence length of the light source (typically $30 - 50$ μm for a high-power SLD). For the all-fiber assembly used for the test cases presented in this thesis, there is a relatively large difference between the theoretical and the measured coherence lengths of ~ 140 μm (see dashed line in Fig. 2.3). This might be due to multiple reflections within the fiber optical interferometer. This broadened peak in the autocorrelation must be considered and so approx. 70 μm can be seen as the lower bound for the spatial resolution of the system.

The distance between the measurement volume and the wall can be adjusted by adjusting the delay of the VDL - independent of the vertical position of the

sensor head. Irrespective of any movement of the surface, measurements are always performed at a set distance from the wall. One could say that the measurement location is in wall-fixed coordinates instead of lab-fixed coordinates as for other techniques.

Each measurement yields the relative velocity between reference surface and particle in the direction of the laser beam. In order to determine the wall-normal and wall-parallel velocity components separately, a second measurement with a different incidence angle is required. This is shown in Fig. 8.2 as measurement beam b. These two measurement do not need to be taken simultaneously and the measurement volumes of the two beams do not necessarily coincide exactly. In fact, their offset will typically vary along the wall-normal direction. Consequently, the beams do not look at the same horizontal position. But the spacing of the beams and their diameter is small and since the resolution in wall-parallel direction is usually not crucial, this should not pose a problem.

Throughout this thesis the laser beams a and b will be indicated with either FORWARD (looking in the upstream direction) or BACKWARD (looking in the downstream direction).

8.2.2 Data Analysis - SR-LDV

Consider the velocity vector $\mathbf{u} = (u, v)$, where u is the wall-parallel velocity and v is the wall-normal component. Assume (without loss of generality) that the bisector of the laser beams from measurements a and b is perpendicular to the wall (as shown in Fig. 8.2). Interference between rays $1a$ and $2a$ produces a peak in the power spectrum at

$$f_a = \frac{2}{\lambda}(v\,cos\alpha + u\,sin\alpha) + f_{AOM} \tag{8.1}$$

(λ is the wavelength of the laser beams). The Doppler shift between rays $1b$ and $2b$ (from a second measurement) occurs with the opposite sign for the u component. The peak is thus at

$$f_b = \frac{2}{\lambda}(v\,cos\alpha - u\,sin\alpha) + f_{AOM} \tag{8.2}$$

Denote the spacing of the two peaks as $\Delta F = |f_a - f_b|$ and the average Doppler shift as $\sum F = \frac{1}{2}(f_a + f_b) - f_{AOM}$. The velocity vector is then obtained from

$$u = \frac{\lambda \Delta F}{4 sin\alpha} \qquad \text{and} \qquad v = \frac{\lambda \Sigma F}{2 cos\alpha} \tag{8.3}$$

Since α is small, the sensitivity to wall-normal velocities ($\partial \Sigma F / \partial v$) is much larger than to in-plane velocities ($\partial \Delta F / \partial u$). The ratio of the sensitivities is $1/tan\alpha$. This is desirable, because the wall-normal velocities are much smaller than the wall-parallel velocities in boundary layer types of flows.

In order to relate the sign of the shift of the beat signal, $f - f_{AOM}$, to the flow direction, one has to account for the setting and for the design of the interferometer. With an interferometer design as shown in Fig. 8.1, consider a case where the light reflected off the particle is more blue shifted, i.e., $f_2 > f_1$ (where f_1 and f_2 are the frequencies of rays 1 and 2, respectively, as shown in Fig. 8.1). When the interferometer is set such that the path lengths match when ray 2 passes through the AOM and ray 1 passes through the delay arm, i.e., to a negative delay, the beat note will have the frequency $(f_{AOM} + f_2) - f_1$. When, on the other hand, ray 2 passes through the delay arm and ray 1 is frequency shifted, the beat note will have the frequency $(f_{AOM} + f_1) - f_2$. For both scenarios the shift of the beat signal has opposite signs. The same case with an interferometer design where the AOM is included in the delay arm, will lead to beat signal shifts in the opposite direction.

It has been assumed that the orientation of the sensor head to the surface is known. Lacking the orientation of the wall relative to the detector the flow direction relative to the wall cannot be obtained. In this case only the flow velocity components along directions aligned in relation to the sensor head can be determined. Another assumption was that the wall is stationary. When the wall moves relative to the sensor head, the measured velocities are relative to the wall speed.

8.3 Self-Referencing Laser-Two-Focus Velocimetry (SR-L2F)

8.3.1 Measurement Principle - SR-L2F

The key features of this technique are the same as for SR-LDV, namely low coherence velocimetry with spatial self-referencing capability. Now, however, two laser beams are used to measure a single velocity component. The standard laser-two-focus principle is based on the measurement of the time of flight of a particle between two light gates. The light gates are formed by two highly focused laser beams, which allow the detection of relatively small particles. The lengths of the focal regions are usually still several hundred micrometers, which limits the spatial resolution in the beam-wise direction. Also, the absolute location of the focal region relative to an object is not known, only the relative distance to the focusing optic. Using low coherence light and an interferometer setup resolves both limitations. Only particles, which pass at a certain distance from the wall across the focal region produce a beat signal.

The changes to the SR-LDV experimental setup are twofold: first, the three-port polarization independent circulator is replaced by a four-port polarization dependent circulator. It provides two independent beams of perpendicular polarization. The incoming light from these two ports is directed into the interferometer.

Furthermore, in the SR-L2F setup both laser beams are set perpendicular to the surface. Therefore, no Doppler shift is generated by wall-parallel velocities. The extraction of velocity data follows the common L2F analysis techniques (see Chapt. 3.3), except that it derives the data from the beat signals. The measured velocities are then relative to the sensor head. In addition, the system is sensitive to out-of-plane velocities by detecting the Doppler shift, as in SR-LDV.

Consider Fig. 8.3 and assume the interferometer is set to a delay of $2d$. Two virtual coherent volumes in the beam waists of focus a and b are generated. The thickness of these volumes is only defined by the light source and is about half of the coherence length. Reflections from particles within the coherent volumes are indicated as ray $2a$ and ray $2b$, reflections from the surface as ray $1a$ and ray $1b$. Interference is only possible between light of equal polarization, see Chapt. 2.2 and 1.1.3. Since the four-port polarizing circulator separates the rays a and b by perpendicular polarization, only light of ray $1a$ and ray $1b$ or $2a$ and $2b$ is able to interfere. Hence each volume is independent, but at the same distance d from the surface.

8.3.2 Data Analysis - SR-L2F

As described in Chapt. 3.3 the time of flight t_f of particles passing the light gate of two laser beams, i.e., beam a and beam b, is determined. Therefore both common analysis methods, the correlation method and the histogram method, can be used.

As input signal only the filtered beat signal will be considered, see Fig. 8.4. It contains all events where interference occurs, i.e., where particles are within a thin volume of a focus at a certain distance d from the reference, in that case the surface. The unfiltered signal contains information about all particles passing the focal points, trace 2. It is like a shadow signal, particles in the foci block the reflected light from the surface, which decreases the signal level.

Due to the orientation sensitivity of the L2F method, the direction of the velocity vector $u = (u, w)$ is given inherently. Another important difference to SR-LDV is that all wall-parallel velocities are measured independently of any surface movement. Thus, these velocity values are not referenced with the surface velocity, but related to a lab-fixed coordinate system. The u velocity component can be determined with

$$\mathbf{u}_{ab} = \frac{l_{ab}}{t_f} \tag{8.4}$$

It is also possible to obtain the out-of-plane component v of a general velocity vector $u = (u, w, v)$ at the same time. Following Eq. 8.3 the v velocity depends on the cosine of the incident angle relative to the normal of the surface. In case this angle is zero (the sensor head was assumed to be perpendicular to the surface) Eq. 8.3 can be simplified to

$$v = (f - f_{AOM}) \cdot \frac{\lambda}{2} \tag{8.5}$$

with f as the Doppler frequency of the peak power in the spectrum, f_{AOM} as the center frequency of the optical modulator and λ as the light wavelength. Due to the similarity to SR-LDV, the value of the v velocity component is also measured with respect to the movement of the surface.

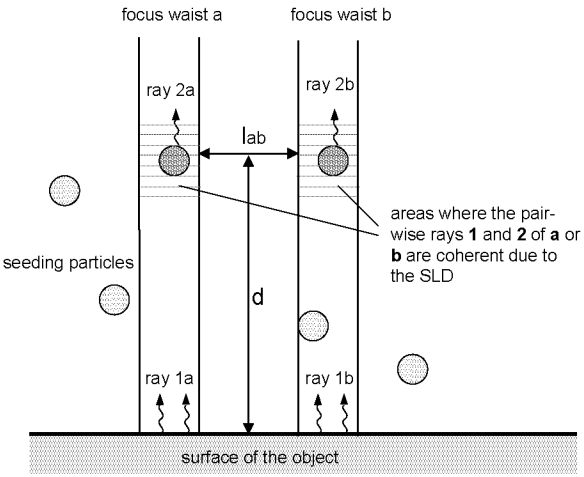

Fig. 8.3: Self-referencing L2F principle.

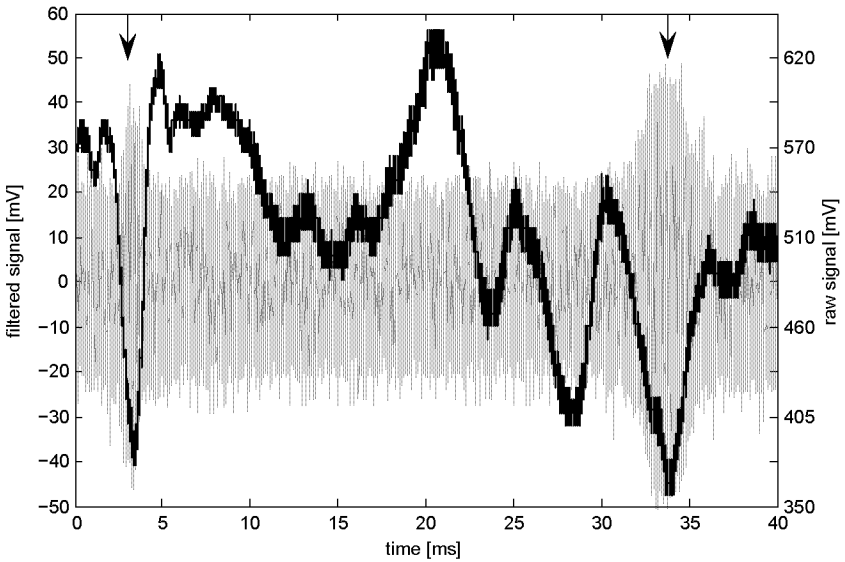

Fig. 8.4: Particle passages: bandpass filtered signal (gray), raw signal (black) - the relevant events are indicated by arrows [12].

[12] Please note: the raw signal is first bandpass filtered and then amplified, thus both signal values are not directly comparable.

9 Experiments

9.1 Signal Processing

Fig. 9.1 shows the data acquisition chain for the velocimetry experiments. The analog signals from the photoreceiver are first filtered by a bandpass filter (Mini Circuits BBP-60) and then amplified by 36 dB with a high speed amplifier (Hamamatsu C5594-12). The preconditioned signals are then digitized with 8 bit precision by a

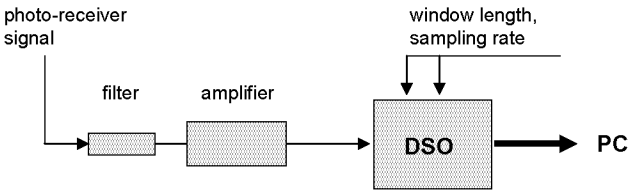

Fig. 9.1: Data acquisition - boundary layer profiler.

Digital Storage Oscilloscope - DSO (LeCroy LT347L). The data is finally transferred to a PC for further analysis and storage. The sampling rate and the acquisition window length are set through the DSO. The data acquisition is triggered by a particle passing the laser beam at the correct distance from the reference surface, i.e., when the bandpass filtered signal exceeds a threshold (see also Fig. 8.4). The dips in the unfiltered signal during relevant particle passages (indicated by arrows) were caused by a partial blockage of ray 1 through the particle. The subsequent data analysis was performed by a LabView program (Ver. 7.1, National Instruments).

For the SR-LDV measurements, the raw data is first bandpass filtered with a second-order Butterworth IIR-filter. Then the power spectrum of the signal is calculated with the standard LabView Fast-Fourier Transformation - FFT algorithm. Next, from the power spectrum the frequency information of a particle passage is extracted by the LabView peak detection routine. The threshold for the peak detection is manually adjustable, as well as the number of points used to interpolate the position of the frequency peak. Typical settings used during the experiments are 10 points for the interpolation routine and a threshold twice as high as the noise level. Finally the frequency data is converted into velocity as described in Sect. 8.2.2.

In the L2F routine, after the bandpass filtering, the signal envelope is determined by a Hilbert transformation and another lowpass filtering step. Signals above a certain threshold are then indicated with 1 and below the threshold with 0. Next, this binary signal is autocorrelated. In the autocorrelation function all peak positions

are detected with the LabView peak-detection routine. Furthermore, the distribution function of the time of flight data is determined with histogram method. Finally, with the knowledge of the light gate spacing, the time of flight is converted into velocity data (see Sect. 8.3.2).

9.2 Measurements in Liquid Flows

9.2.1 Poiseuille Flow - Rectangular Channel

The tests in a closed rectangular channel were primary realized to demonstrate the performance of the measurement system under controlled conditions. Also the comparison to the theoretical profile should be established. In addition, the velocity profile within the channel was measured in the SR-LDV and in the SR-L2F mode, providing similar but in the way of the analysis routine independent data (frequency vs. time of flight measurement).

The dimensions of the channel are 20 mm by 3.3 mm with a length of approx. 500 mm. Optical access was possible through the channel walls (Plexiglas, 1.5 mm thick). In both measurement configurations the sensor head was placed approx. 6 cm above the channel and the diameter of the coupling lens was 5 millimeter. At the back side of the lower Plexiglas wall a retro-reflecting foil was affixed (see Fig. 9.2). The orientation of the channel was horizontal. Oil (Bizol, CGPL-68) was sucked through the channel at constant flow rates. As seeding aluminum powder with particles sizes of approx. 50 microns was used.

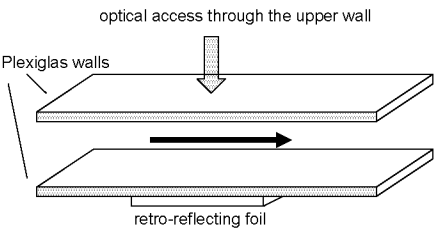

Fig. 9.2: Optical access - rectangular channel experiment.

With the retro-reflector it was possible to obtain good reflections, also at high incident angles (needed for the SR-LDV measurements). In that way the reference reflection was not directly the channel bottom. Hence, the optical delay set in the interferometer representing the bottom of the channel is not zero. The relative measurement positions in the channel were recalculated under the consideration of the refractive index of the oil and the mentioned offset.

Fig. 9.3 shows the comparison of the three flow profiles (parabolic theory, SR-LDV, SR-L2F). In the SR-LDV measurements the observation angle was $\pm 14^o$, indicated with either FORWARD or BACKWARD. The optical delay in the autocorrelator (Chapt. 5, Fig. 5.1) was set to positive values. Therefore, the observed beat signals are smaller than the AOM frequency for the forward setup and higher for the backward setup at positive flow directions. The error bars for SR-LDV representing the minimum and maximum velocity out of 30-50 measurements for each position. The standard deviation is with approx.

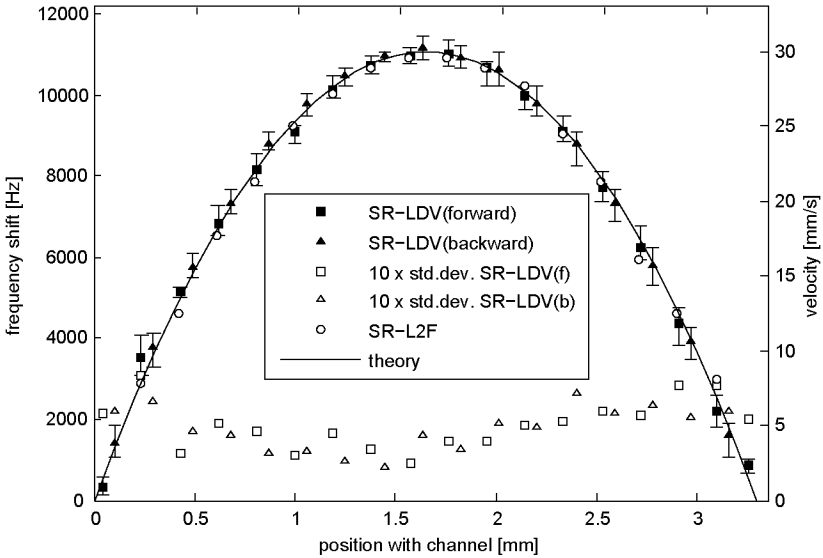

Fig. 9.3: Poiseuille flow profile measured with SR-LDV and SR-L2F, $Re \approx 2$.

0.5 mm/s (200 Hz) nearly constant over the profile. All data was obtained at a sampling rate of 50 MHz and with a measurement window of 100 k samples. Thus, the resolution of the power spectrum in this test was 500 Hz. At the highest velocity, a particle passage almost covered the acquisition window. Undersampling shifted the beat signal to 5 MHz. For the L2F measurement the plotted velocity at each position is always related to maximum in the histogram of class occurrences of the time of flight data. Both measurements compared with each other and compared to the theoretical parabolic profile show a good agreement.

9.2.2 Couette Flow - Rotating Cylinder

The measurements between two coaxial rotating cylinders, i.e., Taylor-Couette flow, were performed to demonstrate the self-referencing capabilities. A metal cylinder (outer diameter $2r_i = 83$ mm) was placed coaxially in the center of a Plexiglas cylinder (inner diameter $2r_o = 89.3$ mm, 5 mm thick). The length of both cylinders is approx. 30 cm, they were installed vertically. The resulting gap, of about 2.85 mm, was filled with olive oil and aluminum powder (particle size ≈ 50 μm) as seeding. The inner cylinder could rotate with frequencies of up to $\Omega/(2\pi) = 6$ revolutions per second.

The SR-LDV sensor head was located approx. 60 mm radially outside of the outer cylinder and slightly tilted against the flow direction. Due to the beam deflections at the curved Plexiglas surface, the angle of incidence relative to the inner cylinder is

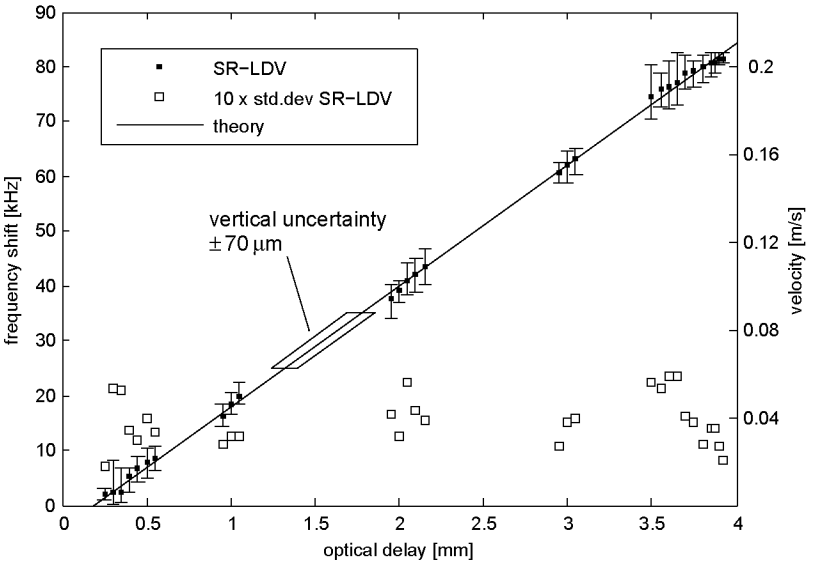

Fig. 9.4: Measured velocity profile of Couette flow at 0.21 m/s surface speed.

not known a priori. It was later calculated to be approx. 15^o, based on the measured frequency shifts near the wall and the known rotation rate. For these flow parameters the flow is laminar and the flow is parallel such that the wall-normal velocity component is known to be zero. Measurements with a single incidence angle are thus sufficient.

A retro-reflecting foil was attached to the inner cylinder (the reference surface). The primary reason for this was to increase the reflection level from the reference surface back into the collimator lens. The reflections from the metal cylinder are otherwise very directional and thus largely miss the collection lens for sufficiently large angles of incidence. The light is not reflected from the surface of the foil, but enters it and is reflected from the internal structures. It thus covers a small path within it. This has the welcome side effect that the (optical) reference surface does not coincide with the foil surface, but lies within the foil. This allows one to measure closer to the reference surface. Normally, measurements at or near the reference surface (within the first 50 to 100 μm) require that the path lengths through both interferometer arms are nearly equal. In that case, however, all other reflections also produce interference with themselves. This results in a high background level of the beat signal, above which passing particles cannot be detected. The offset due to the path length within the reflector foil was measured to be 0.18 mm. Owing to the spatially periodic structure of the retro-reflector, the backreflection level is not constant, but instead highly modulated. It was also observed that, due to a shadowing effect, the reflection level from the retro-reflector and walls decreases during particle passages. However, in the bandpass filtered signal only the beat signals are visible.

In Fig. 9.4 the frequency shift of the beat signal is plotted versus the optical delay of the interferometer. The surface velocity U_S of the inner rotating cylinder was 0.21 m/s. In a coordinate system fixed with the rotating cylinder, the fluid flow direction is negative, i.e., at the stationary outer Plexiglas wall the relative velocity is the highest and at the moving cylinder's surface it is zero, with a linear profile in-between. The error bars represent the minimum and maximum of the frequency shifts out of 10 to 30 particle passages for each position. The standard deviation is between 1 and 2 kHz and nearly constant across the gap. Data with high spatial resolution was obtained close to each surface and within three central regions. Close to the fixed Plexiglas wall the data rate drops rapidly, because the absolute flow speed is close to zero and the number of particle passing the laser beam per unit time decreases. Note that the surface of the inner cylinder corresponds to an optical delay of 0.18 mm, the optical path within the retro-reflector.

Fig. 9.5 shows the frequency shift of the beat signal versus the optical delay of the interferometer at different rotation speeds of the cylinder. The data series are labeled by the surface speed of the rotating cylinder and the corresponding Taylor number (η as the dynamic viscosity)

$$Ta = \frac{\sqrt{r_i}\omega\,(r_o - r_i)^{3/2}}{\eta} \tag{9.1}$$

The maximum rotation speed of this test setup was approx. 6 Hz, corresponding to a surface velocity of $U_S = 1.55$ m/s. The data at all rotation speeds shows a linear behavior in accordance with theory. Fig. 9.6 shows the range of the measured

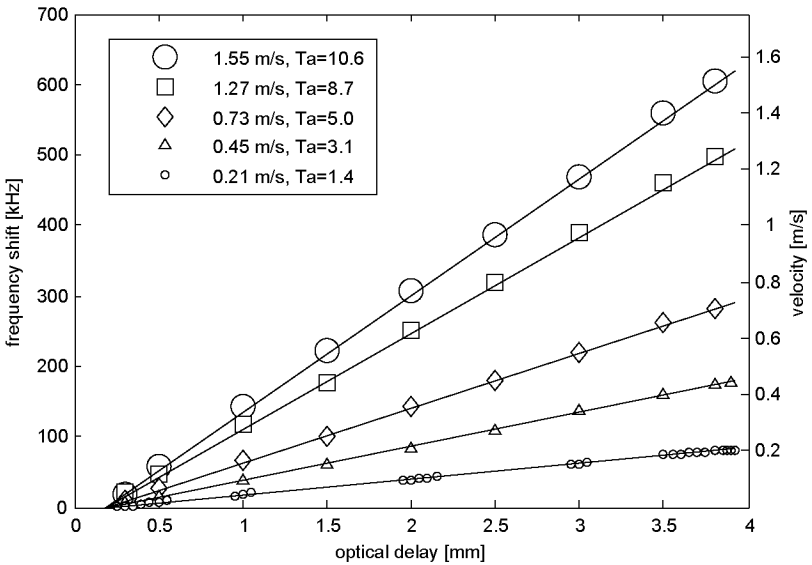

Fig. 9.5: Measured velocity profiles of Couette flow at various rotation speeds.

frequency shifts and the standard deviation for each rotation speed. "Max positive error" refers to the maximum difference between the highest measured frequency shift and the mean, "max negative error" refers to the maximum difference between the lowest frequency shift and the mean. The standard deviations are averaged over the gap, because they are nearly constant for a given rotation speed. The values are plotted relative to the surface velocity. The "U_S-relative" error is with $\sim$ 2% independent of the rotation speed. Assuming that the wall-normal extent of the measurement volume is 70 μm or $\sim$ 0.5% of the gap width, one would expect to see variations of 0.5% of U_S in the particle speed passing the measurement volume. Thus, about one quarter of the standard deviation can be attributed to the finite spatial resolution and the velocity gradient. At all surface velocities, except at 1.55 m/s, the data was obtained at a sampling rate of 50 MHz and with a measurement window of 25k samples. At the highest rotational speed only 5,000 samples have been recorded. Hence, the spectral resolution was 2 kHz and 10 kKHz, respectively.

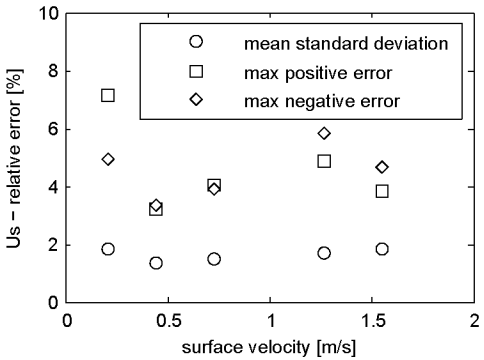

Fig. 9.6: Standard deviation/errors - Couette flow experiment.

The spatially periodic structure of the retro-reflector moving with the rotating cylinder caused a temporally periodic signature in the recorded signal. Because this modulation was well outside the expected frequency range from interfering beams ($f_{AOM} \pm \Delta F$), it could be discriminated from the useful signals. It did, however, limit the length over which a single particle passage produces a continuous interference signal. When measuring close to the stationary wall, this modulation limited the duration of the signature of a particle passage. Consequently, the acquisition window was set approximately to this value.

At higher rotations speeds the beat signal length was shorter than the acquisition window, which means that the effective spectral resolution was lower than the theoretical value for a given frequency and the length of the acquisition window. Hence, at the highest surface speed of 1.55 m/s, a shorter acquisition window was used such that the beat signal lengths were again comparable to the acquisition window.

L2F measurements at moving surfaces could not be performed. Due to the measurement principle, single particles have to pass both light gates and a clean reference reflection must be observed during both events. With a modulated reference signal the probability of correlated signals drops rapidly, making L2F measurements impossible. With a mirror-like foil as reflector the reference signal was much more stable, but the data rate for L2F was still insufficient.

9.3 Gaseous Flows

9.3.1 Flow Seeding

For boundary layer investigations in gaseous flows liquid droplets as seeding are not very useful. The main reason is that the liquid droplets easily wet the surface, which in turn affects the boundary layer flow behavior. Better suited for these measurements would be dry smoke, with almost no influence on the surface and the flow. The drawback of smoke seeding is the very small particles sizes, which result in low reflection levels. Since low coherent light sources have relatively low power, smoke is yet not applicable to the interferometric self-referencing technique. As the most practicable seeding material, small solid salt particles have been found. With crystal sizes between 1 and 4 microns, sufficient reflections can be observed. In addition the salt crystals do not contaminate the surface as much as liquid droplets.

The salt crystals are produced by an ultrasonic atomizer which is placed in a NaCl water solution. The membrane of such an atomizer device oscillates at an ultrasonic frequency and causes cavitation within the surrounding fluid. This in turn leads to the formation of small droplets. The size of these droplets is in the order of 1 to 10 microns. As the generated droplets evaporate, a cube-shaped NaCl crystal will remain from each droplet. In a simple setup, the atomizer is placed in a closed bucket. Two flexible PVC-tubes are attached on the lid. At one tube air can be blown in, at the second tube particle-laden air streams out.

The NaCl crystal size can be controlled by the concentration of the solution. Applying the law of mass conservation for a solution droplet with a diameter $d_\emptyset$ and the density ρ_s, the edge length l_e of the sodium chloride crystal cube after the water evaporation can be expressed as

$$\frac{l_e}{d_\emptyset} = \left(\frac{\pi}{6} \frac{\rho_s}{\rho_c} f_m \right)^{1/3} \tag{9.2a}$$

$$f_m = \frac{m_{NaCl}}{m_{NaCl} + m_{H_2O}} \tag{9.2b}$$

with f_m as the mass of solute divided by total mass of solution and ρ_c as the crystal density $\rho_c = 2165$ kg/m^3. The density of the solution ρ_s is a function of f_m.

The particle size distribution for different values of f_m was measured using a laser diffraction based particle size analyzer (Rusch et al., 2006). For an ultrasonic atomizer operating in an almost saturated solution the typical crystal sizes range from 1 to 4 microns.

9.3.2 Blasius Solution - Flat Plate

With the use of a more powerful SLD (Exalos 1320-1111, 1320 nm, 25 mW) it was also possible to perform measurements in an gaseous flow. For these feasibility tests the boundary layer profile over a flat plate was measured. An aluminum plate, approx. 70 mm wide, 30 mm long and 1 mm thick was installed horizontally inside a small wind tunnel. The leading edge of the flat plate was sharpened over 3 mm. The wind tunnel consist of a Plexiglas pipe, 60 cm long, inner diameter $\sim$ 70 mm. A shaped inlet together with a honeycomb structure was used for the flow stabilization at the air intake. At the air outlet a second honeycomb structure was followed by the wind tunnel propeller drive, which worked in suction mode. The test section with the flat plate was in the middle of the tunnel (see Fig. 9.7). As seeding particles the previously described salt crystals were used. They were injected in front of the inlet. To avoid contamination of the laboratory with the salt particles, the open loop wind tunnel discharged into a 5 m long flexible pipe guiding the exhaust air to a vent.

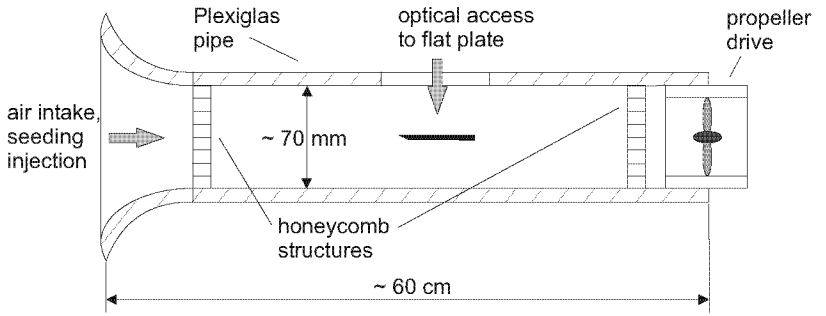

Fig. 9.7: Flat plate wind tunnel schematic.

Optical access was provided through a clear adhesive tape. The tape was stretched across a port hole in the tunnel wall, measuring approx. 30 mm x 80 mm (see Fig. 9.8). The optical sensor head, a focusing lens with a diameter of about 5 mm, was installed above this window at a distance of $\sim$ 6 cm to the aluminum plate.

The focal point of the laser was set close to the surface of the flat plate, simply by focusing until the highest surface reflexion could be achieved. The aluminum surface was slightly roughened in order to obtain good reflections back into the collection lens even at higher incidence angles.

Fig. 9.9 shows the boundary layer profiles measured at three different flow speeds. The plotted data represents the mean value of approx. 20 particle passages for each vertical position. The reference flow rates were measured with a conventional propeller velocimeter (Schiltknecht, model number 12675). The measurement position was 6 mm downstream of the leading edge on the upper side of the plate. The

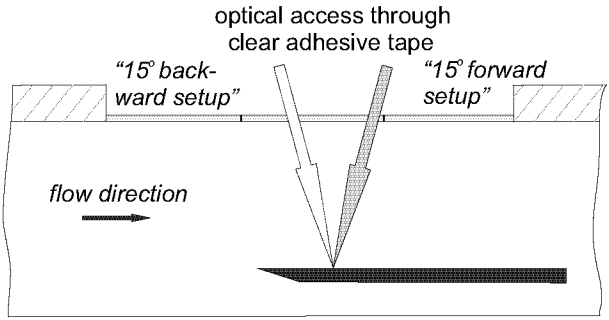

Fig. 9.8: Optical access through clear adhesiv tape, sensor head positioning.

incidence angle was set to $\pm$ 15^o, indicating forward and backward measurement setup (see Chapt. 8.2). After measuring all three flow rates in the forward setup, the sensor head was rotated to the backward setup. In order to investigate the same downstream position on the flat plate, a repositioning of the sensor head was hence necessary.

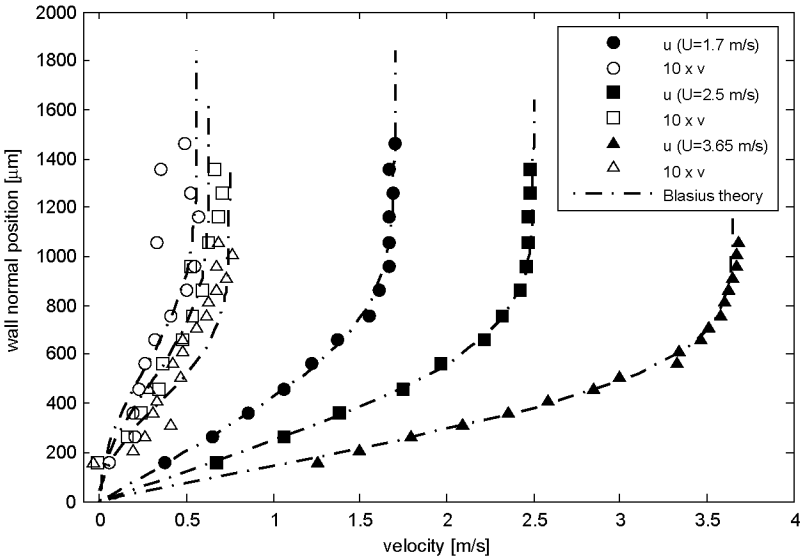

Fig. 9.9: Measured profiles (U = 1.7, 2.5, 3.65 m/s, Re_x = 680, 1000, 1400).

It can be seen that the measured data is in very good agreement with the Blasius theory. It has to be said that the freestream velocity input (measured with the propeller meter) for the theoretical profile calculation was slightly changed (maximum

by ± 0.1 m/s), in order to achieve the best fit with the measured profile. Nevertheless, for the wall-parallel velocity component, only a few points show a small deviation from the theoretical boundary layer shape ($\pm 1\%$). The agreement for the out-of-plane velocity (scaled up in the plot by a factor of 10) is worse, but still satisfactory. Note that the measurement uncertainty (in absolute terms) is independent of the flow velocity. This leads to large relative errors for low flow velocities.

In contrast to the measurements in liquid, no retro-reflecting foil was used to generate the reference reflection. Hence, the zero delay setting of the interferometer is equal to the zero wall normal position. As mentioned before, for measurements very close to the surface this leads to large beat signal due to interference of each signal with itself. Therefore, measurements within the first 150 μm above the surface could not be obtained. Since this value only depends on the light source, but is independent of the flow, the spatial resolution in terms of wall units will depend on the flow. For the intermediate flow speed of $U = 2.5$ m/s ($Re_x = 1000$), this corresponds to $y^+ \approx 3.5$. If desired, it would also be possible to use a retro-reflector in gaseous flows, allowing measurements much closer to the wall. However, compared to aluminum powder seeding used for the measurements in liquids, the salt crystal flow seeding produces a much weaker reflection. Due to this, only reflections of salt particles very close to the focal point produce a detectable signal. In turn, the positioning of the focal point right above the retro-reflector is very challenging as it was done just by hand in these experiments.

10 Measurement Uncertainty Considerations for SR-LDV

10.1 General Measurement Precision

Even though various error sources for laser-Doppler velocimetry are discussed in the literature, e.g., (Durst et al., 1987) and references given there, the overall measurement error for a specific system and for a specific application is not easy to estimate. In addition, to validate a new LDV sensor concept a simple theoretical model might not be feasible. Alternatively, validations are done experimentally by measuring a well known phenomenon and comparing the results with the theory.

For the novel boundary layer profiler this was done with a number of generic flows, i.e., a Poiseuille flow, a Taylor-Couette flow and a laminar Blasius boundary layer over a flat plate. The estimation of the errors in these specific experiments was done under the assumption of a theoretical perfect flow (no turbulence). To compare the test results the optical arrangement of the sensor head was not modified (lens diameter 5 mm, measurement distance approx. 60 mm, observation angle $\pm$ 15^0).

In general, a simple lower limit for the frequency measurement accuracy can be given by

$$\Delta f_{min} \sim \frac{1}{\Delta t} \tag{10.1}$$

where Δt is the length of the observed particle burst. In particular, this could be improved by a factor of about 2 due to the interpolation scheme for the peak detection in the power spectrum. However, this value strongly depends on the experimental setup and cannot be taken as constant. In the following only three sources of error are described, which are significant for the self-referencing setup.

10.2 Aperture Broadening

As shown in Fig. 10.1, the angle of scattered light can vary from $+\beta$ to $-\beta$ depending on the aperture of the collecting lens. Since the Doppler shift of the backscattered light among others also depends on the observation angle (see Eq. 3.2, Chapt. 3.2.2), this results in a broadening of the received Doppler frequency signal. In a first

estimate (see Saarimaa (1979) for experimental validation) the limits of this effect can be determined as

$$\Delta f_{broad} = \pm \frac{2u}{\lambda} sin\beta \tag{10.2}$$

The mean Doppler shift for a reference beam LDV depends on the incidence angle α (see Eq. 3.5)

$$\Delta f_{mean} = \frac{2u}{\lambda} sin\alpha \tag{10.3}$$

One can built the ratio between the broadening effect and the mean Doppler shift

$$\zeta_{broad} = \pm \frac{sin\beta}{sin\alpha} \tag{10.4}$$

Taking the mean Doppler shift as the quantity of interest for flow velocity measurements, this ratio can be seen as the maximum impact factor of aperture broadening onto the measurement value.

10.3 Shadowing Effect

The shadowing effect is a special aspect of self-referencing LDV. Since the reflection from the particle and reference surface are in line outside of the interferometer, a particle crossing the laser beam can hide partially the reflections of the surface during its passage. To make a self-referenced measurement, the light from the particle and from the surface has to interfere to generate a signal. In case of interference, a relatively large signal from the surface can act as an amplifier for the particle reflection. The resulting beat signal, as a measure of the velocity difference between both reflection sources, is thus increased. Therefore, one has to make sure that while a particle passes the focus, sufficient surface reflections are also visible.

Furthermore, there are also consequences for the measurement quantity itself. For example, consider a scenario where a particle covers one half of the collecting lens for the surface reflection (Fig. 10.1 part below solid angle α). The received light from the particle consists of a broadened Doppler spectrum, which is symmetric with respect to the incidence angle α. On the other hand the light from the surface is broadened only by the half, and more important, it is not symmetrical to α, but to $\alpha - \beta/2$.

In case of a moving surface this leads to a shifted beat signal and in turn to a false measurement of the velocity difference between surface and particle. In contrast to the aperture broadening, this effect cannot be compensated by an interpolation mechanism for the frequency determination. The uncertainty scales with a fraction of $1/\beta$, because the possibility of a larger off axis angles β increases with the collection angle of the optics.

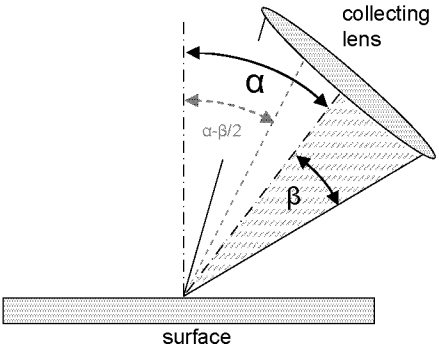

Fig. 10.1: Aperture broadening (black), shadowing effect (gray).

10.4 Frequency Resolution

As mentioned the frequency equivalent Δf_{min} of the length of a given a beat signal defines the limits for the frequency determination. Although the resolution of a calculated power spectrum itself depends on the number of samples of a measurement trace, the accuracy of the frequency determination of a burst signal within this trace is not simply improved by increasing the sampling rate. True resolution improvements are only possible with longer burst signals.

The duration of a signal burst is governed by the time a particle needs to pass the laser beam. Because this time changes linearly with the velocity of the flow, this error source is a relative value. Thus, at low flow velocities the frequency resolution is higher, allowing more accurate velocity measurement (vice versa for high velocities). Besides of the velocity, the passage time of a particle through a laser beam only depends on the diameter of the laser beam and on that of the particle. The larger of which is the determining factor.

Using larger seeding particles increases the passage time and in turn the frequency resolution, as well as the amount of backreflected light from the particles. However, an upper limit for particle sizes is given by their inertia and hence their ability to follow the flow. Changing the acceptance angle of a given collecting lens affects the beam diameter in the focus. A smaller collecting angle produces a larger beam diameter, which in turn increases the particle passage time. On the other hand, a large beam diameter decreases the light intensity in the focus. Together with the smaller acceptance angle, the amount of light received from a particle decreases rapidly. Ideally, the diameter of the laser beam and that of the particles are comparable and as large as possible.

11 Conclusions / Outlook

11.1 Summary

Two optical velocimetry techniques were presented which are based on low coherence interferometry. Both have in common that the extent and the error of the position of the measurement volume are comparable to the coherence length of the light source (tens of micrometers). They also share the features that the measurement location is set relative to a reference surface (which could be the surface of a moving object), that they require particle seeding and that the measurement location can be scanned along a line without mechanical movement of the sensor head. Multiple components of the velocity vector can be measured using a single interferometer and light source.

Both techniques were demonstrated in proof-of-principle measurements for liquids. The measurement range depends on the power of the light source, the reflection levels of the reference surface and the particles (i.e., particle size) and the collection angle of the optics (i.e., lens diameter and distance to the measurement volume). In the first test series a lens with a diameter of 5 mm, a measurement distance of 60 mm (collection angle of approx. 5 deg.), aluminum powder as particle seeding (approx. 50 μm in size) and a 10 mW light source (SLD, Superlum Diodes model SLD56-HP2) were used. This allowed a measurement range of approx. 4 mm, without moving the sensor head. Improvements could be made using a more powerful light source (Exalos EXS1320-1111, 25mW). For measurements in liquids the measurement range was increased by a factor of 2. Hence, the focal point does not need to be located most accurate to the surface, facilitating the handling of the sensor. With the increase in light power, measurements in air could also be demonstrated. With a collection angle of approx. 5^o and small salt crystals as seeding (1-4 μm in size) a measurement range of approx. 2 mm without relocating the sensor head was possible.

Decreasing the collection angle leads to an elongated focal point, which in turn increases the range in which the sensor front end does not need to be moved to collect particle reflections, as well as the absolute measurement range in respect to the surface. It also increases the accuracy of the velocity measurement, due to longer lasting signals. On the other hand it significantly lowers the reflection level from the particles. Due to the autocorrelator setup of the interferometer and the large zero delay signal, measurements within the first 100 microns above the wall could not be achieved directly. With the help of a retro-reflector on the surface, the measurement location indicating the surface could be set away from zero interferometer delay.

Further developments should focus on the handling of the sensor. Although the sensor has self-referencing capabilities, measurements are only possible when the focus is set close to the surface, especially when using small particles as in air flows. To overcome this limitation an auto-focusing optic should be implemented. Further-

more, with the actual SR-LDV single beam setup the incident angle to the surface must be known, which is a direct source of uncertainty.

In the following an alternative dual beam configuration for SR-LDV is briefly described. The basic principle is the same as in the single beam arrangement, but the system should be able to overcome the problems with the unknown incident angle and the large zero delay signal.

11.2 Dual Beam Self-Referencing Laser Doppler Velocimeter

Fig. 11.1 shows the schematic setup of the optical components in the interferometer unit of the proposed dual beam self-referencing system. A light source emits low coherence light into a singlemode fiber. A fiber-optical isolator protects the sensitive light source from backreflections and guides the light to a polarization insensitive optical circulator. The circulator is used to transfer the light through a singlemode optical fiber to the a beamsplitter, where the light is split into two parts of equal intensity (denoted with rays a and b).

The light is guided through singlemode fibers to two coupling lenses in the sensor head, lenses l_a and l_b. The length of fiber a ($l_{f,a}$) differs by design from that of fiber b ($l_{f,b}$) by a value Δl, which must be significantly longer than the coherence length or any spatial quantity to be considered for a measurement (say, 10 cm).

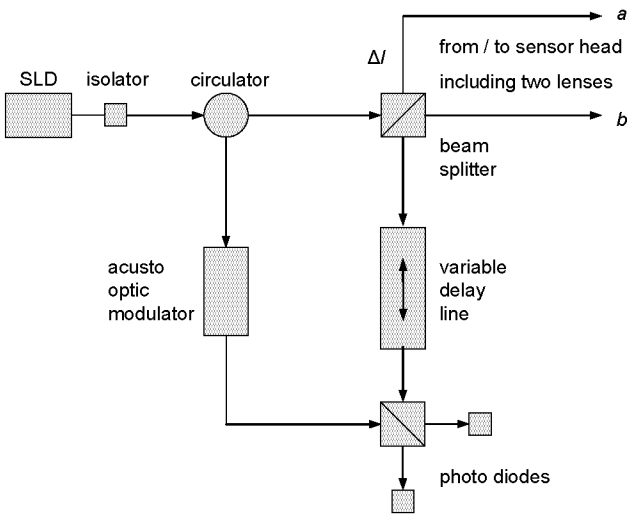

Fig. 11.1: Dual beam self-referencing LDV interferometer design.

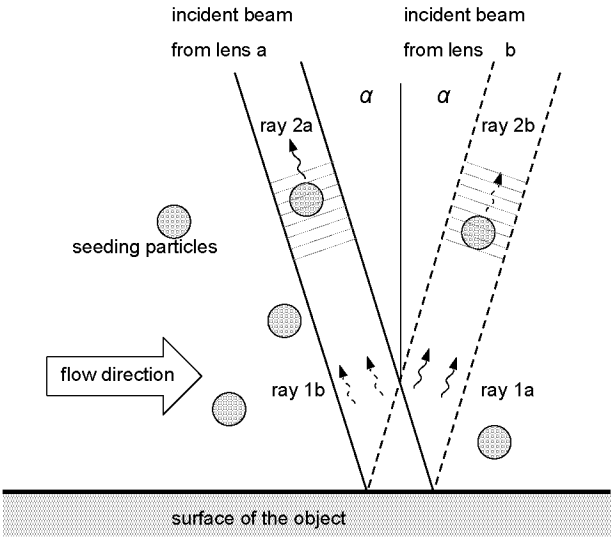

Fig. 11.2: Dual beam self-referencing LDV principle.

Following the nomenclature of Fig. 11.2, light reflected off the test object surface is denoted as rays $1a$ and $1b$ and the light scattered off the particles in the flow is denoted as rays $2a$ and $2b$. All light backreflected and collected by both lenses is guided back to the beam splitter. There one half of the rays 1 and 2 is deflected to the circulator and then into the reference arm including a acousto-optic modulator. The other half is fed into the variable delay arm of the interferometer. The light from the two interferometer arms is finally recombined by another beam splitter/combiner and a broadband photoreceiver serves as detector. In addition, there is an option for a second photoreceiver to increase the SNR.

It is assumed that both lenses have the same incidence angle to the surface, just with an opposite sign, and that the surface is more or less reflective. For laser beam a, as shown in Fig. 11.2, the light travels through the fiber a and is then focused through the lens l_a onto the surface. There, part of the light a is deflected as ray $1a$ to the lens l_b. backreflections from a particle, ray $2a$, will be collected by the lens l_a. For laser beam b this will be vice versa, i.e., a surface reflection ($1b$) is collected by the lens a and a particle reflection ($2b$) by lens b.

However, all reflections (rays $1a$, $1b$, $2a$, $2b$) are now split into the two interferometer arms. Before the interferometer, the pathlength of rays $1a$ and $1b$ is the same and equal to the length of the fiber a plus the fiber b and two times the distance sensor head to surface d_{hs}. The pathlength of ray $2a$ is twice the length of fiber a plus the distance to the particle d_{hp}. Finally, the pathlength of ray $2b$ is twice the length of fiber b plus the distance to the particle. Since the lengths of the fibers

differ by Δl this can be summarized as

$$l_{1a} = l_{1b} = 2\,l^* + \Delta\,l \tag{11.1a}$$

$$l_{2a} = 2\,(l^* + \Delta\,l) - 2\,d^* \tag{11.1b}$$

$$l_{2b} = 2\,l^* - 2\,d^* \tag{11.1c}$$

with

$$\begin{aligned} \Delta\,l &= l_{f,a} - l_{f,b}, \\ l^* &= l_{f,b} + d_{hs}, \\ d^* &= d_{hs} - d_{hp} \end{aligned} \tag{11.2}$$

Setting the variable delay in the delay arm of the interferometer, various combinations of the subpairs of rays are possible. Thereby, only at a few the pathlengths are equal and interference occurs. The following table gives a summary.

interferometer setting	subpairs with equal pathlength
$l_{delay} = l_{ref}$	subpairs interfere with their counterpart and surface reflections ray $1a$ and $1b$
$l_{delay} = l_{ref} + 2\,l^*$	$2b(delay)$ with $2a(ref)$
$l_{delay} = l_{ref} - 2\,l^*$	$2a(delay)$ with $2b(ref)$
$l_{delay} = l_{ref} + l^* + 2\,d^*$	$2b(delay)$ with $1a(ref)$, $1b(ref)$
$l_{delay} = l_{ref} + l^* - 2\,d^*$	$1a(delay)$, $1b(delay)$ with $2a(ref)$
$l_{delay} = l_{ref} - l^* + 2\,d^*$	$2a(delay)$ with $1a(ref)$, $1b(ref)$
$l_{delay} = l_{ref} - l^* - 2\,d^*$	$1a(delay)$, $1b(delay)$ with $2b(ref)$

Table 11.1: Combinations of the ray subpairs with equal pathlengths.

The procedure for data analysis of the dual beam SR-LDV is quite similar to the analysis of the two independent measurements of the single beam SR-LDV (see Chapt. 8.2.2). If interference between a surface reflection and a particle reflection is present, the difference of the Doppler shift frequency can be seen in the beat signal. However, the different optical setup in the front end has to be considered in order to relate the shift of the beat signal, $f - f_{AOM}$, to the velocity components of the particles in the flow.

First, consider the wall-parallel velocity component u only and assume a flow direction as shown in Fig. 11.2. The light backreflected from the particles contains a Doppler shift (rays $2a$ and $2b$). For the light rays $2a$ the Doppler shift is negative ($f_{2a} = -2u/\lambda)sin\alpha$) and for the rays $2b$ it is positive ($f_{2b} = 2u/\lambda)sin\alpha$). The light deflected from the surface does not contain a Doppler shift. This is also true if the surface is moving in u direction, because the light from the surface is deflected from one lens to another with opposite angles. Therefore, this system measures the wall-parallel velocity with respect to the sensor head.

For the wall-normal velocity component v, the system follows the descriptions given Chapt. 8.2.2, which means this velocity component is measured relative to the surface.

The orientation of the sensor head to the surface is inherently known, since sufficient surface reflections are only collected if the sensor head is oriented perpendicular to it.

Appendix

Bibliography

AA-Opto-Eelectronic (2003). Appliation Notes Do you know Acousto-optics? http://www.a-a.fr/Documentation/AO_Doc.pdf. Technical report, last visited Sept. 2006.

Albrecht HE Borys M Damaschke N Tropea C (2003). Laser Doppler and Phase Doppler Measurement Techniques. Springer Verlag Berlin Heidelberg New York.

Alphonse GA Gilbert DB Harvey MG Ettenberg M (1988). High-power superluminescent diodes. Journal of Quantum Electronics 24:2454–2457.

ALSTOM Power (2006). GT24 and GT26 Gas Turbines - 188MW and 281MW. http://www.power.alstom.com. last visited June 2006.

Barranger JR Ford MJ (1981). Laser Optical Blade Tip Clearance Measurement System. J. Eng. Power 103(2):457–460.

Behr T Kalfas AI Abhari RS (2006). Unsteady Flow Physics and Performance of a One-and-1/2-Stage Unshrouded High Work Turbine. ASME Paper No. GT2006-90959.

Böhm R Overbeck E (2005). Power as High as Lasers With the Optical Spectrum of a LED. Laser+Photonics 5:28–30.

Booth TC (1985a). Turbine Loss Correlations and Analysis. VKI Lecture series 1985-5. Von Karman Institute, Rhode-St-Genese.

Booth TC (1985b). Importance of Tip-Clearance Flows in Turbine Design. VKI Lecture series 1985-5. Von Karman Institute, Rhode-St-Genese.

Büttner L Czarske J (2001). A multimode-fiber laser-Doppler anemometer for highly spatially resolved velocity measurements using low-coherence light. Measurements Science and Technology 12:1891–1903.

Büttner L Czarske J (2003). Spatial resolving laser Doppler velocity profile sensor using sightly fringe systems and phase evaluation. Measurement Science and Technology 14:2111–2120.

Cho HH Rhee DH Choi JH (2000). Heat/Mass Transfer Characteristics on Turbine Shroud with Blade Tip Clearance. ICHMT Turbine-2000, Book of Abstracts, No. 32.

Coutsoukis P (2006). India Origin and Development. http://www.photius.com/countries/india/economy/. last visited Oct. 2006.

Dhadwal HS Kurkov AP (1999). Dual-laser probe measurement of blade-tip clearance. Journal of Engineering for Gas Turbines and Power 121:481–485.

Durst F Melling A Whitelaw JH (1987). Theorie und Praxis der Laser-Doppler-Anemometrie. Braun, Karlsruhe.

Durst F Zanoun ES (2002). Experimental investigation of near–wall effects on hot–wire measurements. Experiments in Fluids 33:210–218.

Durst F Zanoun ES Pashtrapanska M (2001). In situ calibration of hot wires close to highly heat–conducting walls. Experiments in Fluids 31:103–110.

Force Inc. (2006). Types of Optical Fiber. http://www.fiber-optics.info/articles/fiber-types.htm. last visited Sept. 2006.

Geisheimer J Billington S Burgess D (2004). A microwave blade tip clearance sensor for active clearance control applications. AIAA Paper No. 2004-3720.

Goodman JW (1988). Statistical Optics. John Wiley & Sons, Inc.

Gusmeroli V Martinelli M (1991). Distributed laser Doppler velocimeter. Optics Letters 16:1358–1360.

Häggmark CP Bakchinov AA Alfredsson PH (2000). Measurements with a flow direction boundary-layer probe in a two-dimensional laminar separation bubble. Exp. Fluids 28:236–242.

Hecht J (2006). A Short History of Fiber Optics. http://www.sff.net/people/Jeff.Hecht/history.html. last visited Sept. 2006.

Huang D Swanson EA Lin CJ Shuman JS Stinson WG Chang W Hee MR Flotte T Gregory K Puliafito CA Fujimoto JG (1991). Optical coherence tomography. Measurements Science and Technology 254:1178–1181.

Inphenix, Inc (2004). Superluminescent Light Emitting Diodes: Device Fundamentals and Reliability. http://www.inphenix.com/pdfdoc/Application_Notes_for_SLEDs.pdf. Technical report, last visited July 2006.

Kaliske R (1996). Geschichtliches und Aktuelles der Optik. 1. Staatsexamen Lehramt, Theoretische Kernphysik, Universität Hamburg.

Lakshminaryayana B (1985). Tip Clearance Effects in Axial Turbomachines. VKI Lecture series 1985-5. Von Karman Institute, Rhode-St-Genese.

Ligrani PM Bradshaw PH (1987). Spatial resolution and measurement of turbulence in the viscous sublayer using subminiature hot-wire probes. Exp. Fluids 5:407–417.

Lin HJ Perlin M (1998). Improved methods for thin, surface boundary layer investigations. Exp. Fluids 25:431–444.

Mandel L (1959). Fluctuations of Photon Beams: The Distribution of the Photo-Electrons. Proc. Phys. Soc. 74:233–243.

Masters BR (1999). Early Development of Optical Low-Coherence Reflectometry and Some Recent Biomedical Applications. Journal of Biomedical Optics 4:236–247.

Meinhart CD Wereley ST Gray MHB (2000). Volume illumination for two-dimensional particle image velocimetry. Measurements Science and Technology 11:809–814.

Pfau A (2003). Loss Mechanisms in Labyrinth Seals of Shrouded Axial Turbines. ETHZ Thesis No. 15226.

Pfister T Büttner L Czarske J (2005). Laser Doppler profile sensor with sub-micrometre position resolution for velocity and absolute radius measurements of rotating objects. Measurements Science and Technology 16:627–641.

Rooth RA Hiemstra W (2001). A Fiber-Optic Tip-Shroud Deflection Measurement System. J. Eng. Power 123(2):359–362.

Rusch D Kempe A Rösgen T (2006). Seeding of high temperature air flow. Experiments in Fluids, submitted 04-06.

Saarimaa R (1979). A laser Doppler velocimeter for surface velocity measurement. J.Phys.E. 12:600–603.

Schaub UW Vlasic E Moustapha SH (1993). Effect of tip clearance on the performance of a highly loaded turbine stage. AGARD-CP-537 Paper No. 29.

Schlichting H Gersten K (2000). Boundary-Layer Theory. Springer Verlag Berlin.

Schodl R (1991). Laser Transit Velocimetry. Von Karman Institute for Fluid Dynamics LS 1991-05 Laser Velocimetry, Rhode Island.

Sheard AG ODonnell SG Stringfellow JF (1999). High temperature proximity measurement in aero and industrial turbomachinery. Journal of Engineering for Gas Turbines and Power 121:167–173.

Sieverding C (1985). Tip-Clearance Effects in Axial Turbomachines. Lecture series 1985-5. Von Karman Institute, Rhode-St-Genese.

Sjolander SA (1997). Secondary and Tip-Clearance Flows in Axial Turbines. VKI Lecture series 1997-1. Von Karman Institute, Rhode-St-Genese.

Steiner A (2000). Techniques for blade tip clearance measurements with capacitive probes. Measurements Science and Technology 11:865–869.

Superlum Diodes Ltd (2005). Performance Sheet SLD-56-HP Very-High-Power SLDs at 1310 nm. http://www.superlumdiodes.com/pdf/56hp.pdf. Technical report, last visited Oct. 2006.

Tomlins PH Wank RK (2005). Theory, developments and applications of optical coherence tomography. Journal of Physics D 38:2519–2535.

UDT Sensors Inc. (2006). Photodiode Characteristics. http://www.udt.com. last visited June 2006.

van de Hulst HC (1981). Light Scattering by Small Particles. Dover, New York.

Wolff S Brunner S Fottner L (2000). The use of hot-wire anemometry to investigate unsteady wake-induced boundary-layer development on a high-lift lp turbine cascade. Journal of Turbomachinary 122:644–650.

Yeh Y Cummins HZ (1964). Localized Fluid Flow Measurements with an He-Ne Laser Spectrometer. Appl. Phys. Letters 4:1768–178.

Epilogue

Between 1997 and 2002 I was studying mechanical engineering with a focus in aerospace technology, turbine engines and rocket propulsion at the Technical University of Dresden. This study included an internship at ABB Corporate Research Ltd, Switzerland. There, I was involved in the development of a new electronic domestic gas meter, which gave me first insights into sensor technologies. Later, in my diploma thesis at the ETH Zurich I made feasibility studies for a new optical tip clearance sensor. This not just opened me the doors to the field of optic measuring techniques, but it also gave my the opportunity for my doctoral study. So I could work on the development of a sensor from the first idea to a working prototype.

In that project I was working together with ALSTOM Power at the new tip clearance sensor, where we could perform first proof-of-principle tests at an ALSTOM large-scale power plant gasturbine GT26. It was the first time the tip clearance has been monitored with high temporal resolution. A modified version of the sensor system will be built at ALSTOM Power. Maybe in the future it will become an integral part of gasturbines with options to active clearance control.

At the same time I was working on another project, namely self-referencing velocimetry. The working interferometer system from the tip clearance sensor should be used for some kind of flow velocimetry. Today low coherence interferometry is not very common in flow velocimetry. This might be due to an actual lack of power of broadband light sources compared to narrowband lasers. In medicine, optical coherence tomography has become a standard technique since many years. This might be due to the fact that optical power must be limited anyway in order to not damage the tissue.

For velocimetry applications I have utilized a key advantage of low coherence interferometry when using a reference outside of the interferometer and thereby making the system self-referenced with respect to it. With this for example, boundary layer measurements at irregularly moving surfaces can be easily obtained. First feasibility tests have been done with the system in liquids and in air. With a rise of power in broadband light sources in the near future, I think self-referencing velocimetry can become a powerful tool for boundary layer investigations.

Personally, summarizing my doctoral study at ETH Zurich I can look back to 4 years full of interesting experiences. Be it the ups and downs in the research itself, the testing at this hell of a machine GT26 at ALSTOM, the teaching assistance of a class with 200 students or the interesting journey to Pasadena.

Curriculum Vitae

Andreas Kempe

Personal Data

date of birth	September 7, 1977
place of birth	Zwickau, Germany
citizenship	German

Education

2006	PhD examination, ETH Zurich, Zurich/CH
2003	Visiting Researcher, California Institute of Technology & Viosense Ltd. Pasadena/USA (4 months)
2002	PhD Student (supervisor Prof. Dr.-Ing. T. Rösgen), ETH Zurich, Zurich/CH Degree Dipl.-Ing. Maschinenbau, Vertiefung Luft-/Raumfahrttechnik, TU Dresden, Dresden/D Diploma thesis, ETH Zurich, Zurich/CH
2001	Internship, ABB Corporate Research Ltd, Baden/CH (9 months)
1997	Study of Mechanical Engineering with focus in Aerospace Technology, TU Dresden, Dresden/D
1996	Military duty paratroopers, Merzig/D University-entrance diploma, Clara-Wieck Gymnasium, Zwickau/D
1993	German secondary school, Clara-Wieck Gymnasium, Zwickau/D
1985	School, Polytechnische Oberschule Biel, Zwickau/D